A numerical study on the hydrodynamic and thermal effects of microscale liquid flows past microstructures

by

Andrew Jacob Tworek

A thesis submitted to the graduate faculty

in partial fulfillment of the requirements for the degree of

MASTER OF SCIENCE

Major: Mechanical Engineering

Program of Study Committee:
Francine Battaglia, Major Professor
Michael G. Olsen
Alric P. Rothmayer

Iowa State University

Ames, Iowa

2004

Graduate College
Iowa State University

This is to certify that the master's thesis of

Andrew Jacob Tworek

has met the thesis requirements of Iowa State University

Signatures have been redacted for privacy

DEDICATION

While away from home, attending graduate school, I missed the short-lived lives of my first-born nieces. I regret not being home with my family during those sad days. The work herein is dedicated to my little nieces, Hope and June Goessling. *All I know of them are the prints of their sweet little feet, but when my time on Earth is finished, their uncle they will meet.*

TABLE OF CONTENTS

LIST OF TABLES

LIST OF FIGURES

NOMENCLATURE

$\vec{A}$	surface area vector
D	diameter
$\vec{v}$	velocity vector
t	time
T	temperature
P	total pressure
p	static pressure
h	channel height
J	Jacobian
I	Identity matrix
k	thermal conductivity
E	total energy
u	streamwise velocity component
v	spanwise velocity component
w	cross-stream velocity component
P	cell
R	residual
N	number
Kn	Knudsen number
Re	Reynolds number
Pr	Pradtl number

S	source term
V	cell volume
c	cell center
g	gravitational acceleration
i	unit vector in normal direction
n	order of accuracy
x	streamwise direction
y	spanwise direction
z	cross-stream direction

Greek Symbols

α	volume fraction
η	under-relaxation factor
μ	viscosity
ρ	density
$\overline{\overline{\tau}}$	stress tensor
ϕ	scalar
λ	mean free molecular path
ζ	vorticity

Superscripts

$*$	guessed value
$'$	corrected value

Subscripts

CD	central difference
h	hydraulic
P	cell
UP	upwind
f	face
i	cell index
$iter$	iteration
k	phase
n	normal
nb	neighboring cells
old	old value

Other Symbols

∇	gradient operator
$\nabla\cdot$	divergence operator
Δ	displacement

Abbreviations

CFD	computational fluid dynamics
MEMS	micro-electro-mechanical systems
SIMPLE	semi-implicit method for pressure linked equations
OTS	octadecyltrichlorosilane

ACKNOWLEDGMENTS

Even from 170 miles away, the support from my family was the driving force behind my success. The comforting phone calls and letters of encouragement provided the emotional stability to reach my goal. They never doubted any of my decisions and even helped me overcome some of my own fears in regards to career decisions. To my parents, Frank and Pat, my sisters, Becky and Molly, and my brothers-in-law, Jason and Josh, you all mean the world to me.

Dr. Francine Battaglia provided financial, technical, and moral support throughout the last 3 years of my college career. She was my professor the last semester of my undergraduate career and offered me an summer position in her research group, in which I was introduced to the fascinating world of computational fluid dynamics. Her encouragement led me to enroll in graduate school, where she mentored me through the strenuous last two years. I received a job offer with Lockheed Martin, thanks in part to a wonderful letter of recommendation from Dr. Battaglia. She has been my teacher in so many aspects of my career at Iowa State University, I just cannot thank her enough.

I would like to extend a special thank you to Dr. Olsen and his experimental research group for lending me experimental results to be used in my analysis. My thesis would not have been complete without the validation of my simulations by comparison to the aforementioned experimental results. In addition, all the support I received from the other members of the ISU Computational Fluid Dynamics Center helped me complete my degree. I would like to say thank you to Anup, Jin, Nan, Ross, Farshid, John, Dr. Lee, Wenny, George, Jay, Mao, Madhu, Rahul, Ying, and Dr. Gao. They all welcomed

me to the group and helped provide an enjoyable atmosphere both in and out of the lab. My time at Iowa State was made even more memorable by the additional years in graduate school. I will never forget the friends I have made and the smiles we have shared.

ABSTRACT

A study of hydrodynamic and thermal effects of microscale liquid flows past microstructures is performed computationally in three-dimensional channels. A range of Reynolds numbers (based on mean velocity and hydraulic diameter) from 50 to 1078 is examined along with constant power inputs of 50, 100, and 200 Watts. Adding microstructures to the interior of the microchannel wall creates recirculation regions and vorticity structures which grow with flow rate and enhance the mixing and heat transfer within the microchannel. "Turbulent-like" characteristics are very desirable for micro-electro-mechanical systems, which is a growing industry. In addition, the microstructures increase the surface-area-to-volume ratio while only slightly increasing the pressure needed to drive the flow.

The numerical results of hydrodynamic effects are compared to experiments showing that conventional computational fluid dynamics codes, solving the Navier-Stokes equations derived from continuum theory, accurately model microscale liquid flows under certain conditions. The percent error between the numerical and experimental results increases as the flow rate increases, leading to conclusions about the possible foundation for the discrepancies.

1 INTRODUCTION

1.1 Background

The old saying, "bigger is better," is a statement that scientists and engineers have shown is not necessarily true. The past few decades have brought incredible advancements in the production and function of microelectromechanical systems (MEMS). Microdevices that combine mechanical motions and electrical signals, although small in size, have a wide range of functionalities making them very desirable. Some of the early MEMS success stories include pressure sensors, accelerometers, and inkjet printers. MEMS accelerometers are currently one of the most widely used devices. Most car airbags rely on MEMS accelerometers to control deployment because of their high sensitivity to crash conditions. In addition, car manufacturers enjoy the added benefit of lower material cost. The successes of MEMS have led many to think that there exists a whole world of opportunity yet to be explored.

Some of the new markets in which MEMS are growing include biological devices used in DNA mapping, optical devices that enhance microscopic images, and chemical sensors used for detection of harmful materials [1]. In the interest of national security, research is being performed to produce microbiosensors that can quickly and accurately detect biological warfare agents. Another application is the use of microheat-exchangers in compact air conditioners that could be built into the uniforms of soldiers and firefighters [2]. As new markets arise for MEMS, so do the demands for more efficient and cost effective design and development. The study of microfluidics plays an important role

in the research and development of MEMS. Currently, engineers are putting effort into gaining a better understanding of the fluid behavior on the microscale in order to aid in MEMS design and development.

A more thorough understanding of microfluidics will enable researchers to develop more accurate computational fluid dynamics (CFD) codes. These codes could greatly enhance the production and function of MEMS devices. It is very costly to take MEMS from the design stage of idea conception, through to the prototyping and testing stages, especially if the product does not produce the desired behavior or function effectively. Currently, there are no testing and analysis standards to follow, which ultimately means there are no guarantees of success [3]. The development of microscale CFD codes could greatly reduce the time and money spent in the prototyping and testing, which in turn could make the overall design process more efficient.

1.2 Motivation and Objectives

Traditional CFD codes solve the Navier–Stokes equations which are valid for continuum theory, i.e., physics on the macroscale. Fluid velocities, pressures, densities, and temperatures are just a few common fluid flow characteristics that CFD codes analyze. Since the Navier–Stokes equations were derived for use on the macroscale, the question arises to whether or not these same equations can accurately solve for flow conditions on the microscale. For example, in the derivation of the Navier–Stokes equations, some surface effects are known to be so small that they are neglected. However, since the ratio of surface-area-to-volume is so much larger on the microscale, surface effects may have a more dominant role than on the macroscale [4]. One question that must be answered is how significant do surface effects influence microscale flows? Furthermore, how much accuracy is lost in the solution of a microfluidic problem using CFD codes based on traditional Navier–Stokes equations? These questions need a combination of experimental, theoretical, and computational research to be answered completely.

To date, more success has been made with gas flows, therefore microscale CFD codes for gas flows already exist. The Knudsen number (which will be discussed in detail in Chapter 2) is accepted as an indication of when continuum theory breaks down for gas flows. As the Knudsen number increases to a value above 10, gas flow experiences free-molecule flow and non-continuum theory is used to calculate flow characteristics [4]. On the contrary, microscale liquid flow behavior is still a relatively controversial topic that requires further research. As of yet, an equivalent liquid parameter to the Knudsen number does not exist, therefore, the transition from continuum to non-continuum theory is not well defined.

The primary objective of the research herein is to better understand liquid flow phenomena in microchannels using CFD as a tool. There are a few microfluidic issues that will be explored as part of the research. First, the validity of the governing equations in a CFD code is important, especially for microscale flows where continuum theory may no longer be applicable. Second, surface conditions are critical to ensure that a simulation accurately represents real physics. For example, boundary conditions and surface roughness are under current scrutiny by many researchers. Some experiments have shown that the no-slip boundary condition remains in affect even on the microscale, however other experiments show that significant slip occurs at the fluid-surface boundary under particular circumstances. In addition, conventional theory states that the surface roughness has negligible impact on friction for laminar flow when the relative surface roughness is less than 5% [5].

Numerical simulations will be used to investigate the hydrodynamic and thermal effects in microchannel flows that contain a microstructure or an array of microstructures. The intent is to analyze the flow behavior and determine if the structures and/or thermal conditions enhance mixing. All simulations will be performed using the commercial code Fluent 6.0. As a caveat to using Fluent, the aforementioned surface conditions will be numerically examined and benchmarked with published data to determine their validity

and applicability. The comparisons between numerical and experimental data will help to establish possible limitations of using Fluent 6.0 to simulate microscale fluid flows.

1.3 Thesis Outline

Chapter 2 of this thesis will provide a literature review of past research involving microscale gas and liquid flows in order to outline the development that has been achieved as well as the issues yet to be resolved. Both microscale liquid flow hydrodynamic and thermal effects will be discussed and examined. Chapter 3 includes a discussion on the governing equations, numerical formulation, and microfluidic effects that are of particular interest to the numerical study presented in Chapters 4 and 5. Chapter 4 presents the numerical study of the hydrodynamics of microfluid flow past a microstructure. The numerical results of Chapter 4 are compared to experimental results obtained from microscopic partical injection velocimetry. The comparisons shown in Chapter 4, will provide the background for a completely numerical study in Chapter 5, which presents results for thermal effects of microfluid flow past an array of microstructures. Since the topic of microscale liquid flow is still under intense investigation, many other characteristics need to be examined numerically and experimentally. Chapter 6 concludes with a summary and recommendations for future work.

2 LITERATURE REVIEW

Microfluidics is a topic that is still undergoing intense investigation. There exists a strong understanding of microscale gas flows, however the microscale issues are not yet completely resolved for liquid flows. The chapter herein introduces the topic of microfluidics, as well as some of the flow considerations that necessitate further investigation. The progress made on microscale gas flow theory is discussed, along with on-going studies involving microscale liquid flows. Lastly, examinations of different CFD tools used in microscale flow simulations will be presented.

2.1 Microscale Considerations

Microscale fluid flow is defined as having flow dimensions of less then 1 mm and more than 1 μm [4]. Microscale flows are of great interest to the production and function of MEMS devices. A stronger understanding of microfluidics can aid in the design, testing, and usefulness of future MEMS devices. Microheat-exchangers, micromixers, microaccelerometers, microbio-sensors, and microchemical-sensors are just a few MEMS devices. Although their dimensions are tiny, their impact on society is huge. Such small characteristic dimensions usually result in laminar flows. However, the laminar flow regime is only clearly defined on the macroscale. One question that can help expand the function of MEMS is "Do microscale flows transition from the laminar to turbulent flow regime at low Reynolds numbers?" Experimental, theoretical, and computational work are all being performed to help answer that question. Furthermore, the question arises "Is there a need for microscale CFD codes, or do the conventional CFD codes meet the needs

of the researchers using them?" It will be shown that microscale theory (implemented into CFD codes) exists for gas flows, because there exists a more thorough understanding of gas flow microfluidics. Therefore, the aforementioned questions are directed toward liquid flows on the microscale.

Conventional theory is comprised of the Navier–Stokes equations as they are applied on a continuum basis to fluid flow. Continuum theory treats the fluid molecules as a continuous medium and defines the flow variables (velocities, pressures, densities, and temperatures) everywhere. Non-continuum theory treats the fluid as a collection of molecules and solves the flow variables for individual molecules each moving independently [6]. Non-continuum theory is commonly referred to as molecular kinetic theory, since it treats the motion of each molecule as an individual element. When to apply continuum versus non-continuum theory is one of the issues that is defined for gas flows, yet not fully understood for liquid flows. Further research is needed to understand when to apply non-continuum theory to liquid flows to accurately account for microscale flow characteristics.

The microfluidic characteristics stem from the enhanced influence that fluid-surface interaction has on the microscale fluid flows. The fluid-surface interaction has a greater impact on microscale flow characteristics because the surface-area-to-volume ratio is much larger on the microscale. For example, a macrochannel with a characteristic length of 1 m, has surface-area-to-volume ratio of 1 m^{-1}. Furthermore, the surface-area-to-volume ratio for a microchannel, with a characteristic length of 1 μm, is 10^6 m^{-1} [4]. The larger surface-area-to-volume ratio also creates noticeable changes in the thermal characteristics of microscale flows. For instance, internal forced convection is greatly enhanced in microgeometries [7]. Enhanced convection is just one example of many microscale thermal characteristics that will be discussed in the chapter herein.

2.2 Gas Flows

Microscale gas flows are classified into five different flow regimes. Each flow regime has unique characteristics, yet one common factor is the use of the Knudsen number Kn to define the regimes. Kn is defined as the mean free path λ of the molecules over the characteristic flow dimension L ($Kn = \lambda/L$) [8]. Shown below are the different gas flow regimes and the range of Kn used to differentiate between them [4]:

Eulerequations(neglectmoleculardiffusion) :	$Kn \to 0 \ (Re \to \infty)$
Navier – Stokesequationswithno – slipboundaryconditions :	$Kn \leq 10^{-3}$
Navier – Stokesequationswithslipboundaryconditions :	$10^{-3} \leq Kn \leq 10^{-1}$
Transitionregime :	$10^{-1} \leq Kn \leq 10$
Free – moleculeflow :	$Kn > 10$

As the characteristic dimension decreases the Kn increases, and once $Kn > 10$ the flow is characterized by non-continuum (free-molecule flow) theory. Therefore, knowing the mean free path λ of the working gas allows for a quick calculation to define the flow regime.

Defining slip conditions for gas flows has come about from extensive molecular-based studies including those of Koplik et al. [6] and Lee et al. [9]. The slip conditions for gas flows are factors of microchannel material and surface roughness, which dominate the fluid-surface interaction. In addition, accommodations to CFD formulations have been validated by studies like that of Colin et al. [10]. Their study involved experimental and numerical studies of gas flow through rectangular microchannel, in which they validated the use of a second-order slip flow formulation for flows with $Kn > 10^{-3}$.

Microscale experimental studies are very difficult to conduct, especially when dealing with geometries on the very small end of the microscale. The fact that the mean free path λ is larger for gas flows than it is for liquid flows, is partially responsible for the

success in studying microscale gas flows. A liquid parameter analogous to the Kn does not exist, in addition, the Kn holds no meaning for liquid flows. However, a generalized point can be made by applying the definition of the Kn to a liquid in order to show the characteristic dimension of the geometry must be on the very small end of the microscale in order to reach $Kn > 10$. Therefore, it is simply an easier task for researchers to study non-continuum characteristics of gas flows because these characteristics occur in geometries that are larger and more conveniently examined.

2.3 Liquid Flows

Consistency is lacking when examining the accomplished microscale liquid flow research. Non-continuum behavior has been captured in experimental results, but any combination of flow or geometrical characteristics can be argued as the reason for the transition to the non-continuum regime. It is not uncommon to find published results stating that flow deviated from continuum theory, yet a completely different researcher studying similar liquids in similar geometries may publish results that show no deviation from conventional theory. The increased role of fluid-surface interaction is one aspect of microfluid liquid flows that is agreed upon.

2.3.1 Hydrodynamic surface effects

Surface effects play a very dominant role in microfluid liquid flows because of the aforementioned large surface-area-to-volume ratio. Surface friction and surface roughness effects are presented in the results of an experimental study done by Guo et al. [5]. The microchannels examined ranged in size from a diameter of 128 μm to 180 μm. Their results show that microchannel surface friction induces flow compressibility, which makes liquid velocity profiles flatter and leads to high friction factors and Nusselt numbers. In addition, the microchannel surface roughness was suggested to be responsible for early transition from laminar to turbulent flow while contributing to the increases in friction

factor and Nusselt numbers. Conventional theory states that laminar flows over surfaces with a relative roughness less than 5%, experience such small flow friction that it can be neglected [5]. The relative roughness is defined as ϵ/D_h, where ϵ is the average surface roughness [11]. However, the findings of Guo et al. [5] show that liquid flow over a surface with a relative roughness less than 5% experience enough friction to increase the friction factor up to 25% from conventional theory [5]. Because of the increased friction, the flows exhibited turbulent characteristics even at relatively low Reynolds numbers which belong in the macroscale laminar flow regime.

An experimental study conducted by Xu et al. [12] also focused on the flow friction for liquid flows in microchannels. The study was performed on microchannels ranging in hydraulic diameter from 30 μm to 344 μm. The Reynolds numbers tested ranged from 20 to 4000 covering the macroscale laminar flow regime. The results published by Xu et al. [12] show no deviation from conventional behavior predicted by the Navier–Stokes equations within the dimensions tested. Clearly, the studies of Guo et al. [5] and Xu et al. [12] both examined liquid flow in similar sized microchannels under similar flow conditions, yet one set shows deviation from conventional theory while the other does not.

Xu published results from a theoretical study specifically examining the viscosity of a liquid flowing in a microgeometry [13]. The study not only examined different microchannels effects, but included polarity effects. An assumption that liquids behave like dense gases and disordered solids was employed in the theoretical study, and the results showed that the non-polar liquids do not exhibit any effects on viscosity until the geometric dimensions were sub-micron. On the other hand, the polar liquids in the study showed that the liquid viscosities were affected by channel size, implying that more effort toward developing molecular models for liquids is necessary.

Experiments performed by Koo and Kleinstreuer [14] classified the findings into three groups: entrance effects, wall-slip effects, and surface roughness effects. The entrance

effects showed that the microchannel aspect ratio played a significant role in the flow deviating from conventional theory. Microchannels with a square cross-section had the lowest friction factors for a given Reynolds number, meaning the entrance region was well predicted by conventional theory. However, as the aspect ratio of the microchannel cross-section increased the friction factors increased and the entrance effects were not accurately predicted by conventional theory. The study on wall-slip effects showed that for liquid flows the wall-slip velocity is negligible since the slip velocity was approximately 0.0014% of the free stream [14]. Lastly, surface roughness effects were shown to affect both the friction factor and pressure gradients in microscale liquid flows, and therefore need to be taken into account when examining flow characteristics.

A thorough wall slip velocity study was conducted by Tretheway and Meinhart [15] by performing microscopic particle image velocimetry in rectangular microchannels. Water flow through two different channels was examined. One channel was a clean glass hydrophilic surface while the other was glass coated with OTS in order to create a hydrophobic surface. Hydrophilic materials absorb and interact with water, while hydrophobic materials repel water. The study showed the fluid-surface interaction for a hydrophilic surface to be in great agreement with conventional theory applying a no-slip (zero velocity at the wall) boundary condition. In contrast, a finite slip velocity was captured in the experimental data for the hydrophobic microchannel. The results showed a slip velocity equal to 10% of the free stream velocity, which is significant on the microscale [15].

2.3.2 Thermal effects

Evidence of deviations from conventional heat transfer theory is also a widely examined topic of research. Peng and Peterson [16] examined the effects of geometrical parameters on convection of liquids through microchannels. The experiments showed that thermal flow characteristics were different from those observed in macroscale chan-

nels. Transitions from laminar to turbulent flow regimes were found to occur at Reynolds numbers (based on mean velocity and hydraulic diameter) as low as 300, with fully-turbulent flow being reached at a Reynolds number of 1000 [16]. The small dimension allows for heat diffusion to rapidly take place through the fluids and therefore the flow characteristics are strongly impacted by the addition of heat transfer.

Studies done by Wu and Cheng [17] examined convective heat transfer through silicon microchannels. The Nusselt number values and the apparent friction constant were discovered to depend greatly on the channel geometries. At low Reynolds numbers the results showed that the Nusselt number increased close to linearly with the Reynolds number, however at higher Reynolds numbers the Nusselt number increased very slowly. Wu et al. [17] developed a non-dimensional correlation for Nusselt number and apparent friction that accounts for geometric properties of the microchannels.

Viscous dissipation effects in microchannels were studied by Koo and Kleinstreuer [18] and the results showed that ignoring viscous dissipation could affect the accuracy of flow simulations and measurements in microgeometries. It was found that the viscous dissipation is a function of Reynolds number, Eckert number, Prandtl number, and microchannel aspect ratio. Dimensional analysis showed that the viscous dissipation was not equal in different channels that shared the same flow characteristics. Therefore, the aspect ratio of the microchannels had a strong influence on the viscous dissipation.

Nakayama et al. [19] published a study comprised of the effect geometric uncertainties have on the design and function of microscale cooling systems. As MEMS become more powerful, so do the demands for microscale cooling components. The study examined the small fabrication and assembly uncertainties that could be common occurrences when building microscale cooling packages. It was found that small geometric uncertainties that would not be noticed on macroscale components could greatly reduce the effectiveness of microscale cooling systems. When dealing with such a small characteristic length, every error is amplified and must be addressed before successful operation is achieved.

2.4 Microscale Computational Fluid Dynamics

As experimental results stockpile information about microfluidic effects on hydrodynamics and thermal liquid flow characteristics, the need to incorporate the information into microscale CFD codes grows. Lockett et al. [20] have performed CFD simulations using Fluent 6.0 to predict temperature profiles in rapid heating micro-tubular stacks. The CFD simulations were successfully completed, however validation by comparison with experimental results has not yet been completed. Wang et al. [21] tested the limitations of different CFD techniques on microscale flows. The tests included using general CFD commercial packages that incorporate conventional macroscale theory, microscale specific CFD packages that are still in the conception stage and are yet to be validated, as well as a few partial differential equation solvers which allow the user to formulate his/her own code. All three CFD techniques had successes and failures, therefore re-iterating the point that future validation for microscale CFD is extremely vital to the future use of CFD for microscale flows.

Clearly, a strong argument as to whether or not CFD simulations accurately model microscale liquid flows does not exist. Some researches have had great results under certain microscale flow conditions and geometries, while others have had poor results on very similar microscale studies. Without a CFD code that is widely accepted as having microfluidic effects incorporated into the formulation, the topic will remain controversial. For the numerical studies to follow this research, the commercial package Fluent 6.0 will be used and results will be discussed in full detail.

3 GOVERNING EQUATIONS AND NUMERICAL FORMULATION

When using a commercial CFD package to simulate fluid flows, there are several important choices to be made such as the numerical solver, level of accuracy, grid resolution, initial conditions, and boundary conditions. The work herein uses the commercial package Fluent 6.0 for all simulations. This chapter will provide information concerning the governing equations and how they are discretized within Fluent 6.0. In addition, the numerical formulation is presented. Some of the following information was adapted from the Fluent 6.0 user manual [22]. Finally, a discussion of boundary conditions and surface roughness is presented for water as the fluid medium in order to validate the use of Fluent. Results from numerical simulations are compared to experimental data focusing on the aforementioned microfluidic considerations.

3.1 Governing Equations

The three-dimensional Navier–Stokes equations for flows with heat transfer are the continuity, momentum, and energy equations. The system of equations include five dependent variables: pressure, temperature, and three velocity components corresponding to a coordinate system. The continuity equation for the fluid flow is:

$$\frac{\partial}{\partial t}(\rho) + \nabla \cdot (\rho \vec{v}) = 0 \tag{3.1}$$

where t is time, ρ is the fluid density, and $\vec{v}$ is the fluid velocity. The momentum equation for the fluid flow is:

$$\frac{\partial}{\partial t}(\rho\vec{v}) + \nabla \cdot (\rho\vec{v}\vec{v}) = -\nabla p + \nabla \cdot (\bar{\bar{\tau}}) + \rho\vec{g} + \vec{F} \tag{3.2}$$

where p is pressure, μ is the fluid viscosity, $\bar{\bar{\tau}}$ is the stress tensor, $\vec{g}$ is the acceleration due to gravity, and $\vec{F}$ is the body force. The stress tensor is defined as:

$$\bar{\bar{\tau}} = \mu\left[(\nabla\vec{v} + \nabla\vec{v}^T) - \frac{2}{3}\nabla \cdot \vec{v}I\right] \tag{3.3}$$

where $\vec{v}^T$ is the transpose of the velocity vector, and I is the unit tensor, however the last group of terms on the right hand side of Eq. 3.3 goes to 0 for incompressible flow. The energy equation for the fluid flow involving heat transfer is:

$$\frac{\partial}{\partial t}(\rho E) + \nabla \cdot (\vec{v}(\rho E + p)) = -\nabla \cdot \left[k_f \nabla T + \left[\mu(\nabla\vec{v} + \nabla\vec{v}^T)\right] \cdot \vec{v}\right] \tag{3.4}$$

where E is the total energy and k_f is the fluid thermal conductivity.

3.2 Numerical Formulation

Fluent 6.0 uses a finite-volume method to discretize the governing equations for a numerical solution. Each individual cell is treated as a control volume. The governing equations are integrated over each control volume in order to obtain discrete equations that conserve each quantity on a control-volume basis.

3.2.1 Steady-state

For steady-state simulations, the time dependent terms in the continuity, momentum, and energy are neglected. Discretization can be illustrated by considering the steady-state conservation equation for transport of a scalar quantity ϕ. The following equation written

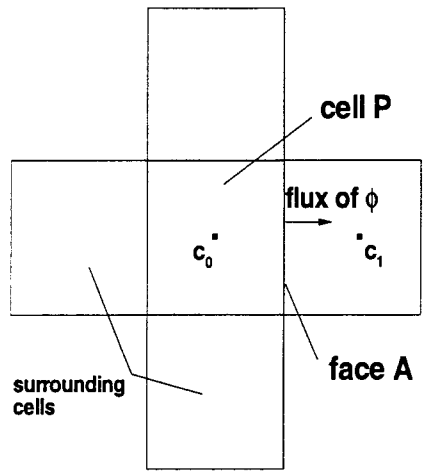

Figure 3.1 Two-dimensional view of finite-volume transport scalar discretization about an arbitrary control volume.

in intregral form over an arbitrary control volume V demonstrates the discretization within Fluent 6.0:

$$\oint \rho\phi\vec{v} \cdot d\vec{A} = \oint \Gamma_\phi \nabla\phi \cdot d\vec{A} + \int_V S_\phi \, dV \tag{3.5}$$

where $\vec{A}$ is the surface area vector, Γ_ϕ is the diffusion coefficient of scalar ϕ, and S_ϕ is the source of scalar ϕ per unit volume.

Figure 3.1 illustrates an arbitrary control volume and shows the scalar transport discretization. Discretizing Eq. 3.5 about the control volume shown in Fig. 3.1 results in the following:

$$\sum_f^{N_{faces}} \rho_f \vec{v}_f \phi_f \vec{A}_f = \sum_f^{N_{faces}} \Gamma_\phi (\nabla\phi)_n \vec{A}_f + S_\phi V \tag{3.6}$$

where N_{faces} is the number of faces enclosing cell P, ϕ_f is the scalar convected through face f, $\vec{A}_f$ is the area of face f, $\rho_f \vec{v}_f \vec{A}_f$ is the mass flux through face f, and $(\nabla\phi)_n$ is the magnitude of $\nabla\phi$ normal to face f. Fluent 6.0 applies Eq. 3.6 readily to any grid, whether the grid is uniform or irregular. The scalar values are stored at the cell centers (c_0 and c_1 in Fig. 3.1), except when solving convective terms, in which case, the cell-centered values are used to interpolate values on the faces.

3.2.2 Segregated solver

Fluent 6.0 provides the option of using a segregated or coupled solver. For the work herein, a segregated solver (using the pressure correction approach) with an implicit formulation was selected to solve the governing equations. The general steady-state equations for continuity and momentum in integral form are:

$$\oint \rho \vec{v} \cdot d\vec{A} = 0 \tag{3.7}$$

$$\oint \rho \vec{v}\vec{v} \cdot d\vec{A} = -\oint pI \cdot d\vec{A} + \oint \bar{\bar{\tau}} \cdot d\vec{A} + \int_V \vec{F}\, dV \tag{3.8}$$

where again I is the identity matrix, $\bar{\bar{\tau}}$ is the stress tensor, and $\vec{F}$ is the force vector.

By integrating over the control volume shown in Fig. 3.1, the discretized form of the continuity equation (Eq. 3.7) is obtained.

$$\sum_{f}^{N_{faces}} J_f A_f = 0 \tag{3.9}$$

where J_f is the mass flux ρv_n through face f. The face flux, J_f, is written as:

$$J_f = \hat{J}_f + d_f \left(p_{c_0} - p_{c_1} \right) \tag{3.10}$$

where p_{c_0} and p_{c_1} are the pressures within the two cells on either side of the face, and $\hat{J}_f$ contains the effects of velocities in these cells.

The same procedure outlined for the scalar transport is used to discretize the momentum equations. For example, the x-momentum equation can be obtained by setting $\phi = u$ as:

$$a_P u = \sum_{nb} a_{nb}\, u_{nb} + \sum p_f A \cdot \hat{\imath} + S \tag{3.11}$$

where subscripts P and nb stand for the cell and its neighboring cells, respectively. The coefficient a_P is a weighting factor. This coefficient is applied to relate the face values of

velocity, $\vec{v}_n$, to stored values of velocity at the cell center. The method is typically called momentum-weighted averaging. Finally, the term d_f in Eq. 3.10 is a function of $\overline{a}_P$, the average of the a_P coefficients for the cells on either side of face f.

3.2.3 Second-order upwind scheme

Another choice to be made is selecting either a first-order or second-order upwind scheme. By choosing the second-order upwind scheme, better accuracy is achieved, however more CPU time is needed. The second-order upwind scheme was used for the discretization of both the momentum and energy equations. In an upwind scheme, face values are calculated from quantities in the cell upstream, relative to the direction of the normal velocity. The scheme computes quantities at cell faces using a multi-dimensional linear reconstruction approach. By this approach, higher-order accuracy is obtained at cell faces using Taylor series expansions of the cell-centered solution about the cell centroid. Thus, when the second-order upwind scheme is applied, the face value ϕ_f is calculated using the following expression:

$$\phi_f = \phi + \nabla\phi \cdot \Delta\vec{s} \tag{3.12}$$

where ϕ and $\nabla\phi$ are the cell-centered value and its gradient in the upstream cell, respectively, and $\Delta\vec{s}$ is the displacement vector from the upstream cell centroid to the face centroid. The gradient $\nabla\phi$ in each cell is computed using the divergence theorem where:

$$\nabla\phi = \frac{1}{V}\sum_{f}^{N_{faces}} \phi_f \vec{A} \tag{3.13}$$

Here the face values ϕ_f are calculated by averaging ϕ from the two cells adjacent to the face. Finally, the gradient $\nabla\phi$ is limited so no new maxima or minima are introduced in the solution.

3.2.4 Central-differencing

The diffusion terms in Eq. 3.6 are discretized using a second-order central-difference method. This scheme calculates the face values for a variable (ϕ_f) as follows:

$$\phi_{f,CD} = \frac{1}{2}(\phi_0 + \phi_1) + \frac{1}{2}(\nabla\phi_{r,0} \cdot \vec{r}_0 + \nabla\phi_{r,1} \cdot \vec{r}_1) \tag{3.14}$$

where the indices 0 and 1 refer to the cells that share face f, $\nabla\phi_{r,0}$ and $\nabla\phi_{r,1}$ are the reconstructed gradients at cells c_0 and c_1, respectively, and $\vec{r}$ is the vector directed from the cell centroid towards the face centroid.

It is well known that the central-difference scheme can produce unbounded solutions and non-physical oscillations which can lead to instabilities in the numerical procedure [23]. Problems with instability can often be avoided if a deferred approach is used for the central-difference scheme. In the deferred approach, the face value is calculated as follows:

$$\phi_f = \phi_{f,UP} + (\phi_{f,CD} - \phi_{f,UP}) \tag{3.15}$$

where UP stands for upwind. In Eq. 3.15, $\phi_{f,UP}$ and $(\phi_{f,CD} - \phi_{f,UP})$ are implicit and explicit parts of the procedure, respectively. As indicated, the upwind part is treated implicitly while the difference between the central-difference and upwind values is treated explicitly. When the numerical solution converges, the approach leads to pure second-order differencing.

3.2.5 SIMPLE method

The SIMPLE method was selected in order to effectively control the coupling between pressure and velocity. SIMPLE is an acronym for semi-implicit method for pressure linked equations [23]. The SIMPLE method is based on a cyclic series of guessed and corrected operations to solve the governing equations [23]. First the velocity field is computed from the momentum equations by guessing the pressure field. Then, the pressures and

velocities are corrected to satisfy the continuity equation. By repeating this procedure, the solution is obtained when convergence is satisfied.

If the momentum equation is solved with a guessed pressure field p^*, the resulting face flux, J_f^*, computed from Eq. 3.10:

$$J_f^* = \hat{J}_f^* + d_f(p_{c_0}^* - p_{c_1}^*) \tag{3.16}$$

does not satisfy the continuity equation. Consequently, a correction J_f' is added to the face flux J_f^* so that the corrected face flux, J_f

$$J_f = J_f^* + J_f' \tag{3.17}$$

satisfies the continuity equation. The SIMPLE algorithm postulates that J_f' be written as:

$$J_f' = d_f(p_{c_0}' - p_{c_1}') \tag{3.18}$$

where p' is the cell pressure correction. The SIMPLE method substitutes the flux correction Eqs. 3.17 and 3.18 into the discretized continuity equation (Eq. 3.9).

3.2.6 Under-relaxation factors

With nonlinear governing equations, it is necessary to control the change of a scalar variable ϕ. To regulate the change of the scalar, an under-relaxation technique has been implemented into Fluent 6.0. The technique decreases the change of scalar ϕ generated at each iteration as:

$$\phi = \phi_{old} + \eta\,\Delta\phi \tag{3.19}$$

Based on Eq. 3.19, the new value of ϕ depends on the old value ϕ_{old}, the computed change of $\Delta\phi$, and the under-relaxation factor, η. The recommended under-relaxation factors for these simulations are 0.3 for pressure, and 0.7 for momentum [22]. For density and

body forces the under-relaxation was set to 1. These are the default under-relaxation values for Fluent 6.0 and used herein.

3.2.7 Residuals in segregated solver

Following discretization using the segregated solver, the conservation equation for a variable ϕ in cell P can be derived as:

$$a_P \phi_P = \sum_{nb} a_{nb} \phi_{nb} + b \tag{3.20}$$

where a_P is the center coefficient, a_{nb} are the influence coefficients of the neighboring cells, and b is the contribution of the boundary condition. In Eq. 3.20, the center coefficient, a_P is defined as:

$$a_P = \sum_{nb} a_{nb} - S_P \tag{3.21}$$

The residual R^ϕ is calculated at every iteration. R^ϕ is the difference between the scalar at the current iteration and the value at the previous iteration. Mathematically, R^ϕ is the imbalance which exists in Eq. 3.20 and when summed over all the computational cells, it can be written as:

$$R^\phi = \sum_{cells\ P} \left| \sum_{nb} a_{nb} \phi_{nb} + b - a_P \phi_P \right| \tag{3.22}$$

To scale the residuals in Eq. 3.22, a scaling factor that represents the flow rate of ϕ is introduced into Eq. 3.22 as:

$$R^\phi = \frac{\sum_{cells\ P} \left| \sum_{nb} a_{nb} \phi_{nb} + b - a_P \phi_P \right|}{\sum_{cells\ P} |a_P \phi_P|} \tag{3.23}$$

For the momentum equations the denominator term $a_P \phi_P$ is replaced by $a_P v_P$, where v_P is the magnitude of the velocity at cell P.

The unscaled residual for the continuity equation is defined as:

$$R^c = \sum_{cells\ P} |\text{ rate of mass creation in cell } P| \tag{3.24}$$

To scale the continuity residual, the right hand side of Eq. 3.24 is divided by the largest absolute value of the continuity residual in the first five iterations as:

$$\frac{R^c_{iter\ N}}{R^c_{iter\ 5}} \tag{3.25}$$

3.3 Microfluidic Effects Along Surfaces

3.3.1 Fluid-surface boundaries

3.3.1.1 Overview

The fluid behavior when in contact with a surface defines the type of boundary condition, for example, no-slip or slip boundaries. The no-slip boundary condition implies that the fluid velocity is zero when in contact with a surface. A slip boundary condition implies that the fluid moves with a finite velocity along the surface, and the velocity is characterized by the stresses imposed at the surface. However, another consideration of the fluid-surface contact resides with the type of surface material. Specifically, the characteristics of water along a surface can be divided into two categories: hydrophilic surfaces and hydrophobic surfaces.

A hydrophilic surface is one that has a strong attraction to water, having a tendency to mix with or dissolve in water. Conversely, a hydrophobic surface is one with a repelling nature that tends not to combine with water. The molecular structure of the surface material is what causes hydrophilic or hydrophobic characteristics. As an example, glass is naturally a hydrophilic surface. However, glass can be treated with octadecyltrichlorosilane (OTS) to create a hydrophobic surface.

3.3.1.2 Description of experiment

In an experiment performed by Tretheway and Meinhart [15], the interaction between water and two different glass surfaces was examined. One channel was uncoated glass creating a hydrophilic surface. The other channel was glass coated with a 2.3 nm thick monolayer of OTS (hydrophobic). The two surfaces provided significant differences in the experimental results. The distinct differences showed that the no-slip boundary condition may not always apply on the microscale, especially for a hydrophobic surface, making it necessary to account for slip when modeling microfluid flows.

The experimental channel was a rectangular duct 8 cm long with a 30 $\times$ 300 μm cross-section. Micro-PIV measurements were taken at a depth of 15 μm in the spanwise direction at an approximate streamwise x-position of 4.5 cm. The flow of water was held constant at a Reynolds number of 336. The x-location of the experiments was a range chosen to allow the flow to reach a fully-developed steady state before micro-PIV measurements were performed. It should be noted that only the experimental data within the first 25 microns from the wall were published.

3.3.1.3 Numerical simulations and discussion

Three-dimensional numerical simulations of water flow in a rectangular duct were performed to compare with the experimental data of Tretheway and Meinhart [15]. There are three options for specifying wall boundary conditions in Fluent 6.0: no-slip, free slip, and specified shear. The no-slip condition was used to compare with the experiments for a hydrophilic surface. In order to simulate microflows within hydrophobic surfaces, the option to specify shear stresses was examined. By changing the specified shear stress, a variety of slip conditions can be imposed at the wall. However, specifying the value of the shear stress is not a realistic numerical practice because slip is the result of fluid-surface molecular interactions and depends on other flow characteristics. In addition, the specified shear is not a constant value along the walls of a three-dimensional channel

since the velocity gradients change with respect to y and z. Modeling slip flow in a two-dimensional channel can be performed rather easily, as long as the flow is fully-developed.

The specified shear for a fully-developed two-dimensional flow is a constant value since the velocity gradient is not changing along the wall. In a three-dimensional channel, the velocity gradient is a function of z along the side-walls, and y along the top and bottom-walls. In other words, specifying shear for a three-dimensional hydrophobic channel requires a specified shear function that is a partial differential equation dependent on y and z. The necessary function has to be found using experimental data and would be specific to only the channel and flow conditions for that particular experiment. Thus for the purposes of validating the numerical simulations for studies involving hydrophilic surfaces, the numerical study of hydrophobic surfaces was unnecessary and therefore, no numerical comparisons for hydrophobic surfaces were performed.

The case examined for benchmarking the numerical simulations was flow in a hydrophilic microchannel, where no-slip boundaries are characteristics of the surfaces. A comparison was made between the experiments, simulations, and the analytical solution for the streamwise velocity profile. The analytical solution is that for fully-developed laminar flow, often referred to as Poiseuille flow, where the known velocity profile is parabolic (refer to Section 4.1.2 for further details). The grid resolution used in the numerical simulations was refined until the percent error between the numerical results and analytical solution was less than 0.4% everywhere. The final grid cell dimensions used in all of the simulations were $4 \times 3 \times 2$ μm^3 ($x \times y \times z$ respectively).

Figure 3.2 shows the agreement between the hydrophilic surface experiment, the three-dimensional analytical solution for fully-developed laminar flow, and the numerical simulations using a no-slip boundary condition. The percent error between the simulations and the experiments for the hydrophilic surface is on average less than 1.2%, however the data points close to the wall ($y \leq 8\mu$m) exhibit larger percent errors up to 18.3%. Discrepancy between numerical and experimental data near a wall is a common occurrence

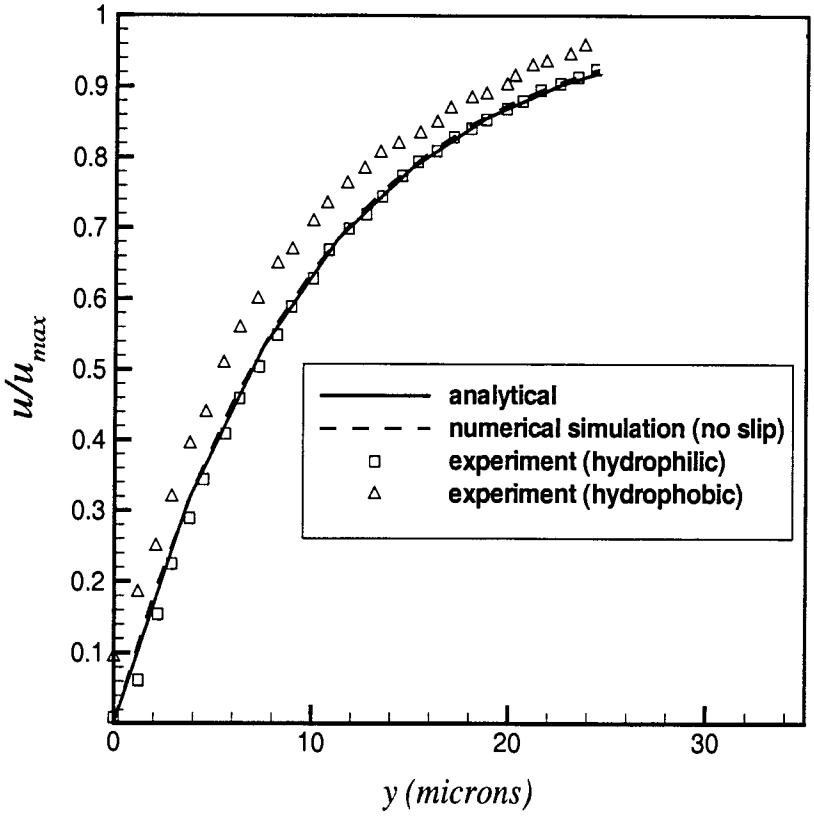

Figure 3.2 Comparison of analytical, numerical, and experimental results [15] examining hydrophilic and hydrophobic surfaces.

when comparing results since a large amount of noise near the wall makes experimental data acquisition difficult.

A noticeable amount of slip is also illustrated in Fig. 3.2 for the experimental results of the hydrophobic surfaces, shown by a finite velocity at the wall. When the glass was treated with OTS, creating a hydrophobic surface, a slip length of approximately 1 micron existed [15]. On the macroscale, a slip of 1 micron would have a negligible effect on the flow characteristics, however in a microdevice, the impact can be dramatic. For the experiment performed by Tretheway and Meinhart, a 1 μm slip length resulted in velocities at the wall that were 10% of the free-stream velocity. Clearly, there exist

situations where the no-slip boundary condition is not sufficient and CFD codes must be altered to account for the different fluid-surface interaction.

3.3.2 Surface roughness

3.3.2.1 Overview

Accounting for surface roughness is a microfluidic issue that is under intense scrutiny. It is standard practice, when performing turbulent flow calculations, to account for friction. For high flow rates, the friction has a considerable impact on the pressure drop which simultaneously has a significant impact on the fluid velocities. On the contrary, it is standard practice to ignore friction for macroscale laminar flow calculations as long as the assumption of "smooth surface" is employed. A smooth surface is defined as having a relative roughness of less than 5% (meaning $(\epsilon/D_h) \leq 0.05$) [11]. Recently, microscale experiments have shown that even small variations in surface roughness may have a noticeable impact on friction, even in the laminar flow regime.

3.3.2.2 Description of experiments

The question of neglecting the surface roughness for laminar flows if the relative roughness is less than 5% was thoroughly examined by Li et al. [5]. Once again the idea of macroscale versus microscale is important. A relative surface roughness of 5% in a large (macro) channel is not large enough to make a difference on the flow friction for laminar flows, however on the microscale a relative surface roughness of 5% could have a tremendous impact on the fluid flow.

The experiments performed by Li et al. [5] examined surface roughness effects in three sizes of constant diameter stainless steel microtubes of diameters 128.76, 136.5, and 179 μm. The fluid examined was deionized water, and measured flow rates and pressure drops were used to calculate friction factors by the relationship:

$$f = \frac{2\Delta pD}{l\rho V^2} \tag{3.26}$$

where f is the friction factor, p is the static pressure, D is the microtube diameter, l is the microtube length, ρ is the fluid density, and V is the fluid velocity [11]. Conventional theory states that for fully-developed steady-state laminar flow in a smooth circular pipe (relative surface roughness less than 5%), the following relationship exists:

$$fRe = 64 \tag{3.27}$$

where Re is the Reynolds number (based on mean velocity and hydraulic diameter) [11].

3.3.2.3 Numerical simulations and discussion

The numerical simulations were performed using the no-slip boundary condition and the fully-developed steady-state velocity profile was compared to the analytical solution. A non-uniform meshing scheme called the Cooper type, creating hex/wedge elements was used. The hex/wedge Cooper scheme is built into Gambit 2.0 which creates a combination mesh of wedge shapes and hexagons with relatively equal size throughout the channel. The final interval size for the hex/wedge elements, which provided great agreement to the analytical solution, was 4 microns. Once the simulations converged to a fully-developed steady-state solution, Eq. 3.26 was used to calculate the friction factor.

As mentioned previously, Fluent 6.0 is designed to solve the traditional macroscale continuity and momentum equations. Therefore, for steady-state fully-developed laminar flow in a smooth pipe, there is no reason to believe the results will vary from the conventional theory shown in Eq. 3.27. Thus, irrespective of diameter size, the friction factor is always $f = 64/Re$, and was verified from the numerical solutions.

Figure 3.3 only shows the numerical results for one diameter pipe simulation because the results are identical for the other 2 pipe diameters. As shown in Fig. 3.3, the numerical simulations verified that $fRe = 64$. However, the experiments showed that for smaller

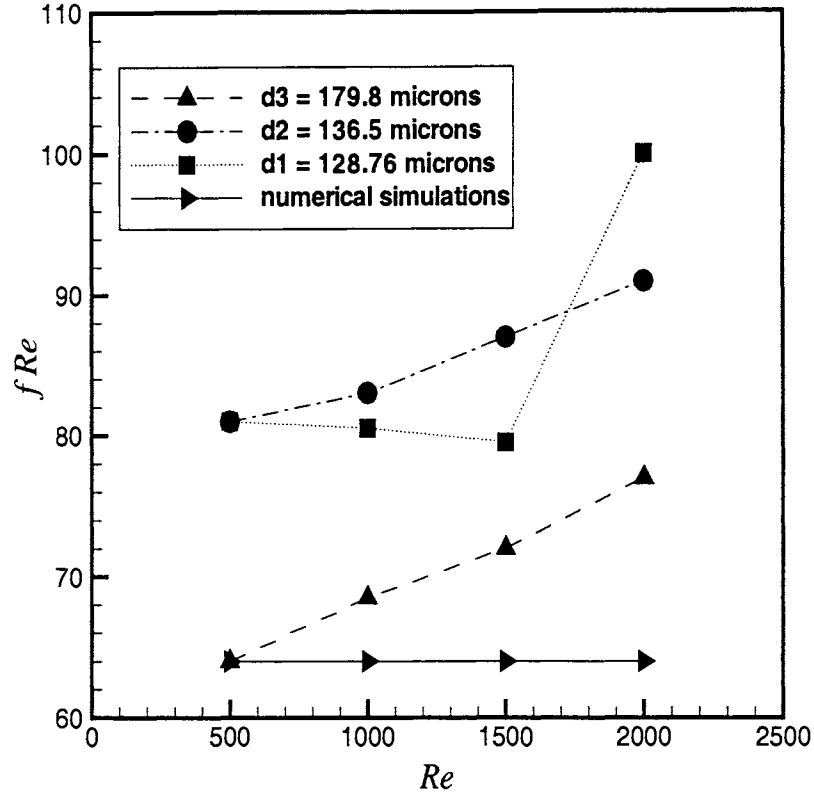

Figure 3.3 Comparison of numerical and experimental [5] results examining friction factors for fully-developed steady-state laminar pipe flows.

diameters, the surface roughness has a large impact on the friction factor, especially at high Reynolds number. The friction factors, based on the experiments, were 10% to 25% higher than the theoretical values for the given range of Reynolds number [5].

3.4 Summary

It has been shown that the type of surface (hydrophilic or hydrophobic) has a significant effect on the fluid flow through a microchannel. In addition, the surface roughness should not be neglected when dealing with Reynolds numbers greater than 500, even

when considering fully-developed steady-state laminar fluid flows with a relative roughness less than 5%. These microfluidic considerations will have an impact on microscale CFD simulations, and further investigation will be greatly beneficial. Thus, based on these findings, Fluent 6.0 will provide accurate results for steady-state microscale laminar flows when the physical surface is hydrophilic (no-slip boundary condition), Re is low, and the channel is smooth. It should be noted that any flow near or beyond a $Re = 500$, there exists a chance of surface roughness effects having a large impact on the flow characteristics.

4 HYDRODYNAMICS OF FLOW OVER A SINGLE STRUCTURE

The large surface-area-to-volume ratio of a microchannel is desirable for industrial applications, especially when heat transfer is important. Smaller spatial dimensions enhance convective heat transfer as the surface-area-to-volume ratio increases. However, decreasing the diameter has an adverse effect on the pressure needed to drive the flow. The pressure required to drive the fluid through a microchannel is inversely proportional to the diameter to the fourth power [2]. One way to increase the surface-area-to-volume ratio, without decreasing the diameter, is to place microstructures on the interior walls of a microchannel. The presence of microstructures also aids in disrupting the flow in order to achieve turbulent characteristics even in the laminar flow regime.

The chapter herein presents the hydrodynamic effects of fluid flow over a single microstructure affixed to the lower interior wall of a microchannel. First, grid resolution is examined to ensure that the best accuracy is obtained with the numerical simulations. The discussion includes analytical solutions used to determine percent error. The remainder of the chapter compares the numerical results of the hydrodynamics of flow over a microstructure with experiments performed in the Experimental Fluid Mechanics Laboratory at Iowa State University. The results will include heat transfer analyses in the following chapter.

4.1 Grid Resolution Study

The numerical studies to follow are for a rectangular microchannel with a constant cross-section of 600 × 165 μm ($y \times z$ respectively), resulting in a hydraulic diameter of D_h=258.8 μm. The channel geometry incorporated a rectangular solid microstructure fixed to the bottom channel wall. Different grid sizes were tested, and each velocity profile was compared to the analytical solution for three-dimensional fully-developed steady-state laminar flow. Fully-developed steady-state laminar flow was named in honor of the man who conducted extensive experimental research on the topic, J. L. Poiseuille [11]. The velocity profiles of Poiseuille flow are easily attainable by use of analytical solutions, as described next.

4.1.1 Two-dimensional analytical velocity solution

Poiseuille flow between infinite parallel plates provides the background for the two-dimensional analytical solution. The fluid streamwise velocity u between infinite parallel plates is only a function of the cross-stream location y, half the distance between the two plates h, fluid viscosity μ, and the pressure gradient $(\partial p/\partial x)$. The two-dimensional analytical solution is shown here [11]:

$$u = \frac{1}{2\mu}\left(\frac{\partial p}{\partial x}\right)(y^2 - h^2) \tag{4.1}$$

The solution to Eq. 4.1 results in a simple parabolic velocity profile, which is shown in non-dimensional form in Fig. 4.1.

As shown in Fig. 4.1, the friction between the fluid and the walls results in zero velocity at the surface boundary (no-slip boundary condition) at y/h for -1 and 1. The fluid viscosity, coupled with the flow rate and pressure gradient, dictates the shape of the parabola. Note that the maximum velocity u_{max} is located at the geometric center of the two plates $(y/h = 0)$, and is related to the mean velocity by:

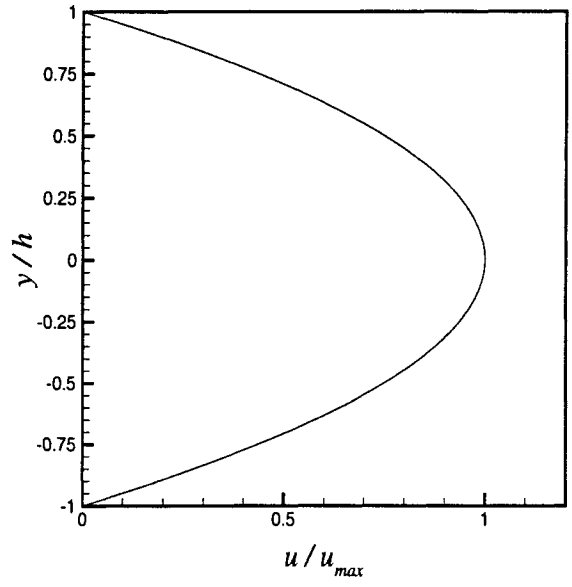

Figure 4.1 Non-dimensional solution to Poiseuille flow between infinite parallel plates.

$$u_{mean} = \frac{2}{3} u_{max} \tag{4.2}$$

4.1.2 Three-dimensional analytical velocity solution

The same principles used to derive the two-dimensional analytical solution are used to derive the three-dimensional analytical solution. However, replacing the infinite parallel plates with a rectangular channel creates a more complex relationship. The three-dimensional analytical solution is a partial differential equation depending on both the y and z position as follows:

$$u(y,z) = \frac{16a^2}{\mu\pi^3}\left(-\frac{\partial p}{\partial x}\right)\sum_{i=1,3,5\ldots}^{\infty}(-1)^{(i-1)/2}\left[1-\frac{\cosh(i\pi z/2a)}{\cosh(i\pi b/2a)}\right]\left(\frac{\cos(i\pi y/2a)}{i^3}\right) \tag{4.3}$$

and,

$$Q = \frac{4ba^3}{3\mu}\left(-\frac{\partial p}{\partial x}\right)\left[1-\frac{192a}{\pi^5 b}\sum_{i=1,3,5\ldots}^{\infty}\frac{\tanh(i\pi b/2a)}{i^5}\right] \tag{4.4}$$

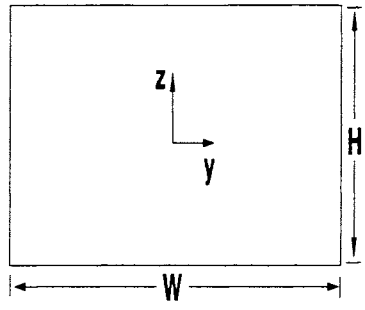

Figure 4.2 Rectangular coordinate system used for 3D analytical solution

where Q is the volumetric flowrate,$-a \leq y \leq a$, and $-b \leq z \leq b$, with $a = W/2$ and $b = H/2$, as shown in the coordinate system in Fig. 4.2 [24].

The velocity distribution of Eq. 4.3 is a three-dimensional paraboloid, with the shape dependent on the aspect ratio of the rectangular channel. Figure 4.3 is a cross-sectional view of the non-dimensional x-velocity contours for the given coordinate system. Figure 4.3 illustrates the effects of the rectangular duct showing that the maximum velocity region (red contours) is dependent on the aspect ratio of the channel forming an ellipsoid pattern. Again, it is seen that the no-slip boundary condition is applied at the fluid surface boundary on all four walls of the rectangular channel, as shown by the blue contour.

4.1.3 Hydrodynamic entrance length

In the simulations to follow, it is necessary to achieve Poiseuille flow upstream of the microstructure in order to examine the influence the microstructure has on the flow characteristics. In addition, the downstream length has to be long enough to regain Poiseuille flow in order to assure that the exit effects do not influence the hydrodynamics upstream, since the exit boundary condition is that of ambient pressure (0 gage). Conventional theory states that the hydrodynamic entrance length $x_{fd,h}$ is proportional to the Re and D_h in the following relationship [11]:

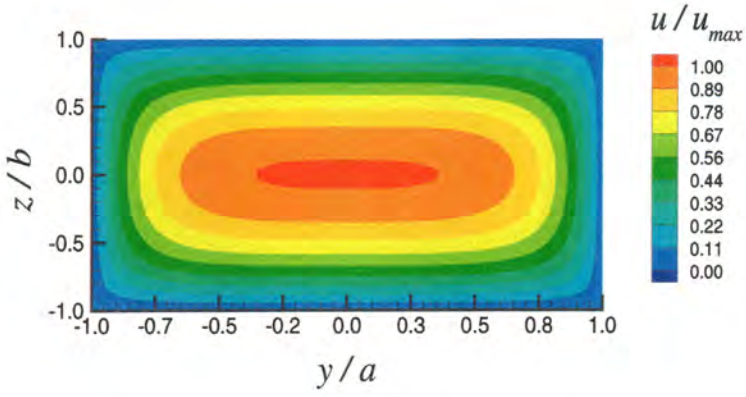

Figure 4.3 Non-dimensional x-velocity contours for three-dimensional analytical solution

$$x_{fd,h} = 0.06 Re D_h \tag{4.5}$$

The relationship shown in Eq. 4.5 was tested to determine if a channel length equal to $x_{fd,h}$ was sufficient for achieving fully-developed flow at the exit. Using a plug flow velocity inlet boundary condition for a channel that was slightly longer than $x_{fd,h}$ for a given Re, it was found that with a fine mesh, the outlet velocity profile was in good agreement with the three-dimensional analytical solution.

As mentioned previously, it is important to ensure that the flow is fully-developed both upstream and far downstream of the microstructure in order to isolate the effects the microstructure has on the flow. Thus, it is important that the entrance length before and after the structure is sufficient. The later is simple in that the velocity profile can be examined near the exit to see if the flow has recovered a fully-developed distribution. The former is more difficult in that the entrance length must be sufficient so that fully-

developed flow is achieved before the influence of the microstructure disturbs the flow field upstream. The velocity profile specified numerically at the channel inlet directly affects how the flow develops. If a plug flow velocity boundary condition is used, then the entrance length must be greater than the analytical entrance length. Although this methods works, adding longer upstream lengths creates a larger computational problem and sacrifices extra disc storage space, as well as computational time. Extra computational space and time are two drawbacks that make the next method more desirable. Instead of using a plug flow inlet boundary condition, a fully-developed velocity profile can be used as the inlet boundary condition. Defining fully-developed flow as the inlet condition assures that Poiseuille flow exists prior to the interaction with the microstructure.

4.1.4 Grid selection

Three issues dictate grid size selection: the available total number of cells, cell aspect ratio, and number of nodes in the shortest channel dimension. Memory allocation and disc space for the simulations herein prevent the total number of cells from being greater than 2.6 million. It is common practice to create cells that have $1:1:1$ ratio of Δx to Δy to Δz. However, when trying to decrease the total number of cells, it is acceptable to increase the cell aspect ratio to 2, but increasing the ratio to 3 is generally bad practice, and can increase the probability of computational error in the results. Lastly, the smallest channel dimension must be considered. For the simulations to follow, the z-direction is the shortest dimension with a length of 165 microns. It is necessary to create enough cells in the z-direction to capture the effects produced by the wall friction.

The first mesh created had the following dimensions: $\Delta x = 15$ microns, $\Delta y = 10$, and $\Delta z = 10$ microns. A grid resolution study followed by decreasing the cell size (one direction at a time) in order to show which direction had the greatest effect. It was found that refining the mesh in the x-direction provided no added accuracy to the solution, however refining in both y- and z-directions increased the accuracy. Doubling

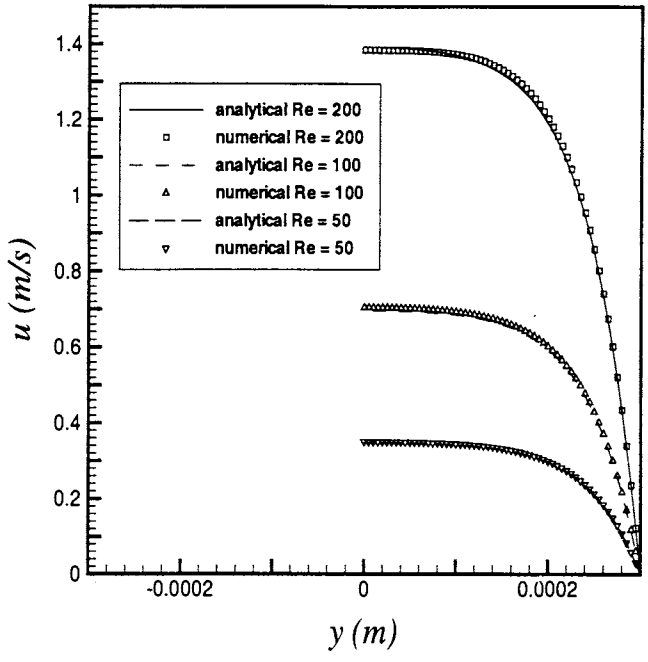

Figure 4.4 Results of final grid resolution test

the number of cells in y- and z-directions, in addition to decreasing the Δx value to 10 microns (to keep the aspect ratio equal to 2) created a mesh that had approximately 1.8 million cells and provided great agreement to the analytical solution.

As shown in Fig. 4.4 for three Reynolds numbers, the percent error between the analytical solution and numerical data is very small. The average percent error for the three curves shown in Fig. 4.4 is 0.7%, with a maximum error of 1.8%. Such a small percent error provides justification for using the cell size $\Delta x = 10$ μm, $\Delta y = 5$ μm, and $\Delta z = 5$ μm. The creation of an acceptable mesh, along with the proper combination of numerical settings (refer to Section 3.2), laid the foundation for acceptable numerical simulations, which are presented in the next section.

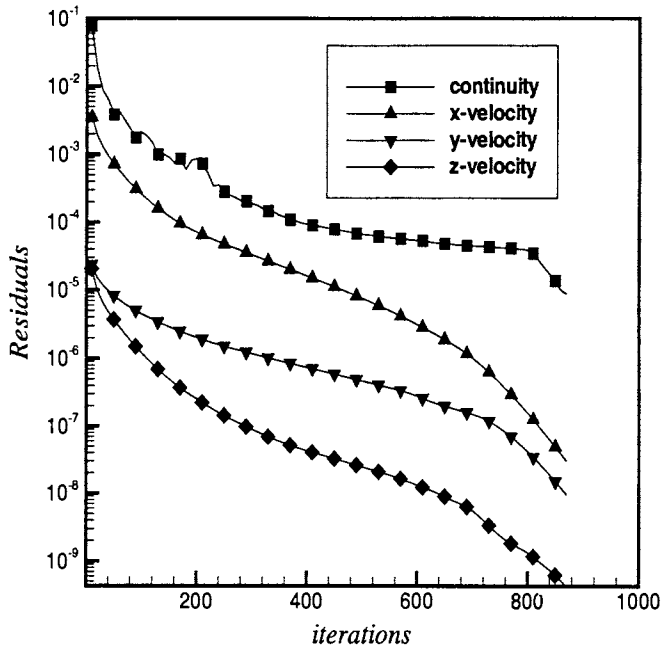

Figure 4.5 Residual plot of grid resolution study simulation

4.1.5 Covergence criteria

The Fluent 6.0 convergence criteria default setting is 10^{-3} for all scalar residuals. In order to achieve a more accurate solution, the convergence criteria was set to 10^{-5} for all scalars. By lowering the convergence criteria it is assured that all the residuals decrease by at least 3 orders of magnitude. Figure 4.5 shows the residual plot for a numerical simulation used in the grid resolution study. It can be seen in Figure 4.5 that the continuity residual takes the longest to reach the set convergence criteria, and therefore dictates the number of iterations necessary to attain a converged solution. The velocity residuals all decrease much more than 3 orders of magnitude but the iterations do not cease until the continuity residuals meet the set criteria. Using Iowa State University's 44 node Intel Xeon cluster, which combines 2.8 GHz dual processors per node, a high speed Myrinet switch for fast MPI communication, and a 100 Mbit Ethernet switch for

fast I/O to the file servers, and running the simulation in parallel with 2 processors, the 878 iterations (shown in Fig. 4.5) took approximately 11 CPU hours.

4.2 Description of Experiments

Microscopic particle image velocimetry (microPIV) was performed on a micrchannel with a microstructure on the interior wall at Iowa State University by Olsen et al. [2]. The channel was 600 μm wide, 165 μm deep, and approximately 4 cm long. The microstructure was a rectangular solid 120 μm wide, 120 μm long, with a height of 43 μm. Figure 4.6 clearly illustrates the dimensions of the channel used for the experiments.

Various cases were tested, where a constant volumetric flow rate was examined for each case. The various flow rates yielded Reynolds numbers based on a hydraulic diameter ranging from 108 to 1078. For a given flow rate, after the flow reached steady-state, images of the fluid flow where captured at six different heights (refer to Fig. 4.7) both at 350 μm and 700 μm downstream of the microstructure. The following section shows the comparison between the computational and experimental results, in order to validate the accuracy of using CFD to simulate microchannel fluid flow.

4.3 Numerical Simulations and Discussion

The geometry used for all simulations was identical to the experimental geometry with the exception that the channel length downstream of the microstructure was shortened to 8 mm (as opposed to 20 mm in the fabricated channel). This shorter length was chosen in an effort to reduce the number of grid cells used in the computations in the streamwise direction. Changing the channel length was necessary due to the large aspect ratio of the microchannel ($x/y = 66$ and $x/z = 242$) which made the simulations computationally intensive for adequate grid resolution. To ensure that the shorter channel length did not adversely affect the flow dynamics upstream, velocity profiles were examined at the exit

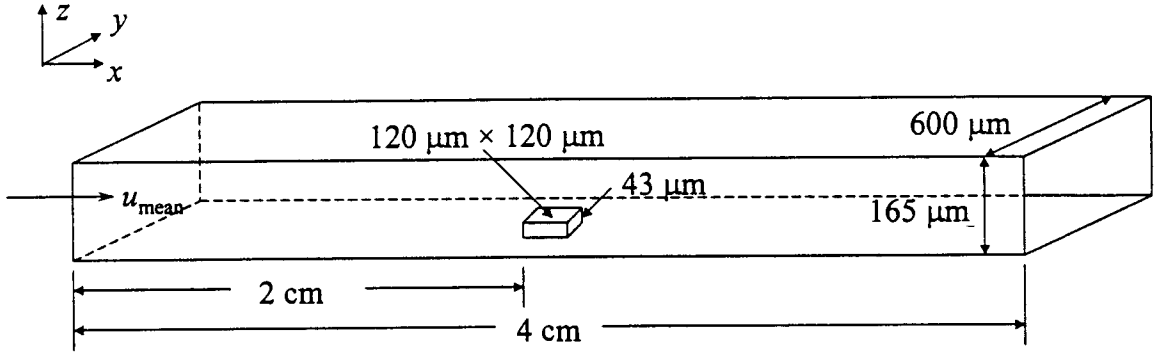

Figure 4.6 Experimental microchannel with microstructure on interior wall

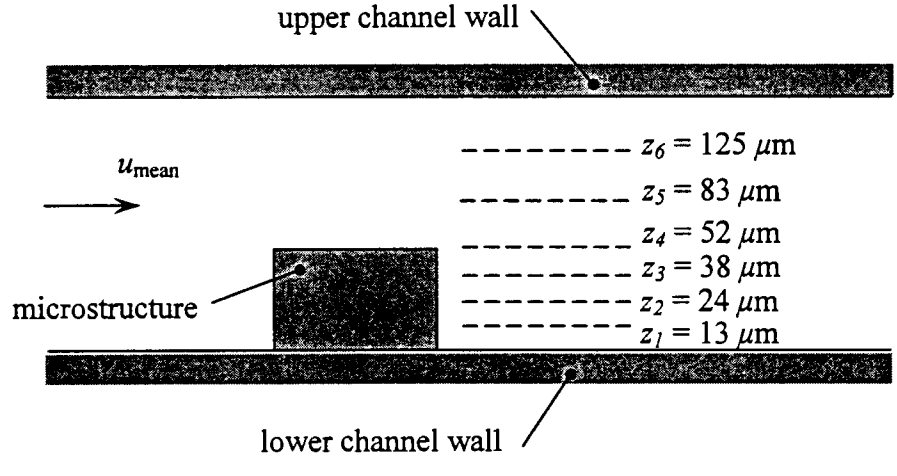

Figure 4.7 Experimental z-locations of the microPIV measurements

to verify that fully-developed flow was recovered in the simulations.

Another flow characteristic that aided in reducing the computational effort was the fact that the experimental data showed the flow was symmetric about the mid-plane (which was expected). The symmetric nature of the flow field in the spanwise direction permitted modeling one-half of the microchannel width (300 μm). Boundary conditions were specified for an inlet velocity profile based on the mean velocity, u_{mean}, and ambient pressure at the exit. A no-slip boundary condition was enforced at all surfaces (hydrophilic material), and a symmetry boundary condition was invoked along the channel centerline.

Figures 4.8 and 4.9 show a comparison between the streamwise velocity profiles at six heights (z) at locations 350 μm and 700 μm downstream, respectively, for the case of Re_{D_h}= 108. The velocity is non-dimensionalized by dividing the velocity at every location by u_{mean}. The y-location is non-dimensionalized by dividing by the channel width W. Due to the symmetric nature of the flow, only the results for half the channel width are present. The presence of the structure is visible in the resulting velocity profiles. At a downstream location of 350 μm the wake effect is shown by the low velocity near the centerline and the higher velocity near y/W=0.3 (location between structure and wall). The velocity field at z_6 shows less wake effect, however the velocity is significantly larger than u_{mean}, which results from the flow having to speed-up when passing over the microstructure due to conservation of mass. At 700 μm downstream the wake is less significant, especially at low flow rates, since the downstream flow is returning toward fully-developed Poisueille flow. The numerical and experimental results show excellent agreement, with a maximum percent error of 5.2% and an average percent error of 2.4%. The percent error was calculated as the difference between the numerical and experimental results, normalized by the numerical results.

Figures 4.10 and 4.11 show the results for a Re_{D_h} = 216. At 350 μm downstream, the wake is most prominent at z_4, which is a location slighter higher than the microstructure,

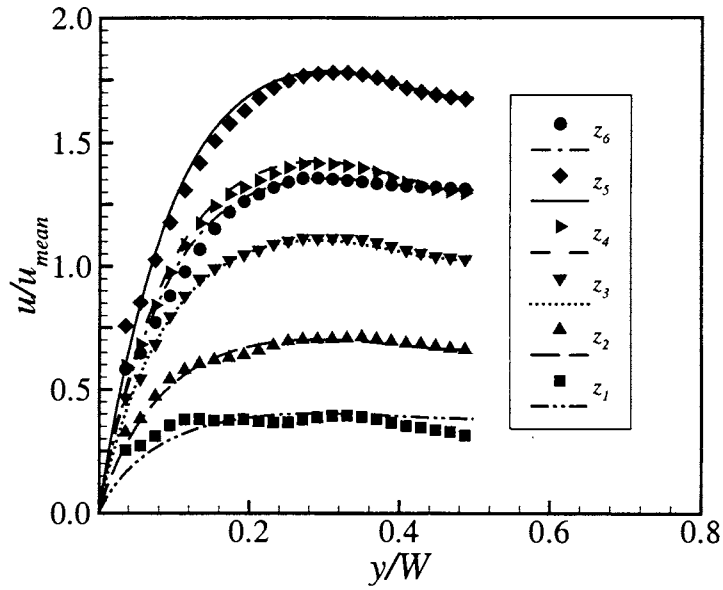

Figure 4.8 Normalized results for Re_{D_h}=108 at 350 μm downstream of microstructure. Experiments - symbols, simulations - lines.

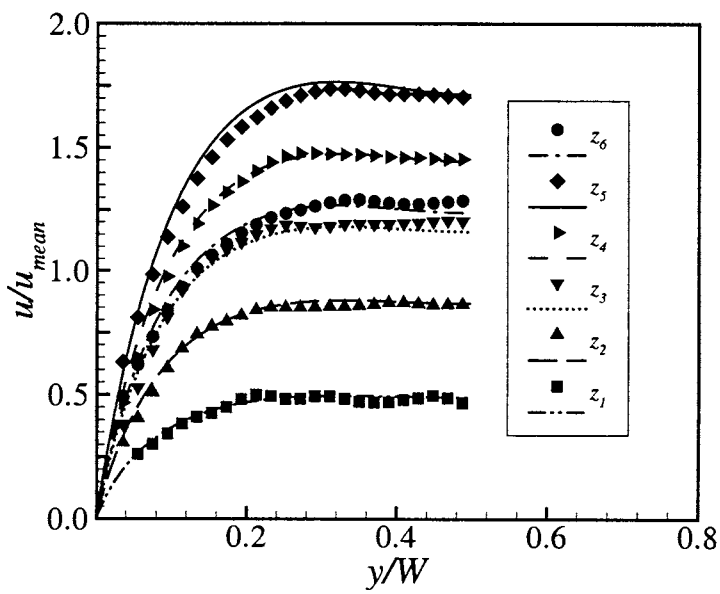

Figure 4.9 Normalized results for Re_{D_h}=108 at 700 μm downstream of microstructure. Experiments - symbols, simulations - lines.

but again the wake effects are almost non-existent at 700 μm downstream. Only at a spanwise location very near the centerline, can any wake effect be seen in the velocity profiles 700 μm downstream. It is clear that at low Reynolds numbers, the flow disturbances are not strong enough to have a noticeable effect at the downstream location of 700 μm. The experimental and numerical results for $Re_{D_h} = 216$ show very good agreement.

Figures 4.12 and 4.13 show a more dramatic wake effect, due to the higher flow rate, Re_{D_h}= 431. The locations below the microstructure height (z_1, z_2, and z_3) and above the structure (z_4) show pronounced wake effects, especially at 350 μm downstream, yet at z_6 the wake is not present. However, at 700 μm downstream, reminents of the wake is captured at z_6, which shows the wake propagates upward as it travels downstream. The agreement between experimental and numerical results is still acceptable at a flow rate of Re_{D_h}=431, however the results show some random locations with higher errors (up to 23%) that make the average error higher than results of lower flow rate cases.

Lastly, Figs. 4.14 and 4.15 show prominent wake effects at all z-locations for 350 μm and 700 μm downstream of the structure. Of course the wake is more prominent at the locations z_1 through z_4, however both locations downstream show the presence of a wake even at z_6. The agreement between the experimental and numerical results is not nearly as good as the lower flow rates. For example, z_4 in Fig. 4.14 shows a discrepancy near the centerline of approximately 30% error. Obviously, the error is not 30% everywhere along z_4, but the fact that the discrepancy grows near the channel center line, creates a higher average error for the entire case.

The growth of the percent error as the flow rate increases could very well be an indication of microfluidic issues contributing to errors in microscale experiments as well as simulations. For example, the laminar flow numerical formulation, within Fluent 6.0, does not account for surface roughness. It was shown (refer to Section 3.3.2) that neglecting surface roughness, even for laminar flow, could lead to increased error in microchannel fluid flows, especially at high flow rates. Clearly, the agreement between experimental and

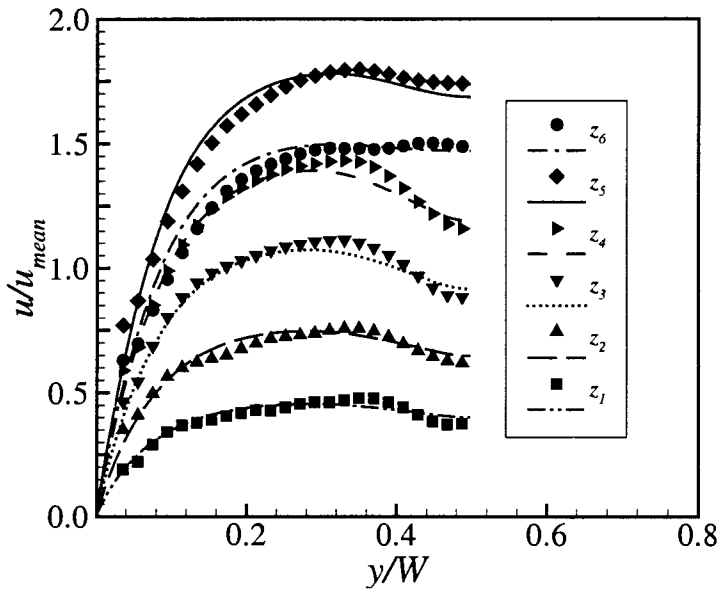

Figure 4.10 Normalized results for Re_{D_h}=216 at 350 μm downstream of microstructure. Experiments - symbols, simulations - lines.

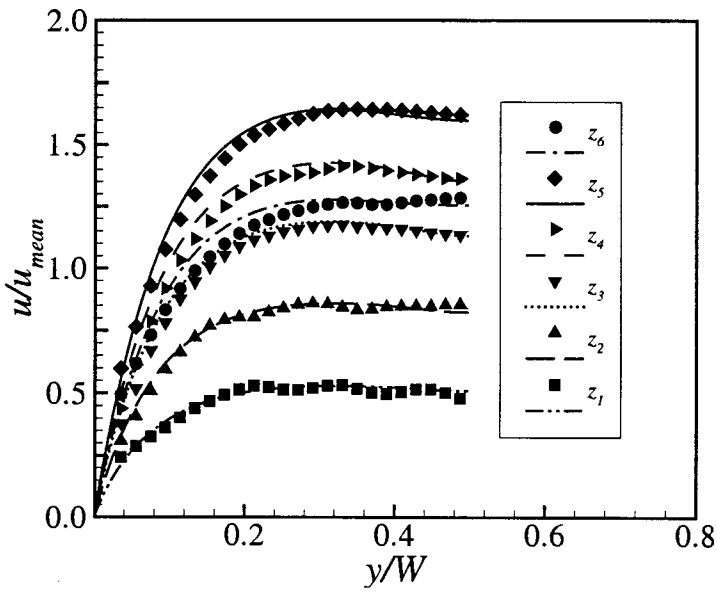

Figure 4.11 Normalized results for Re_{D_h}=216 at 700 μm downstream of microstructure. Experiments - symbols, simulations - lines.

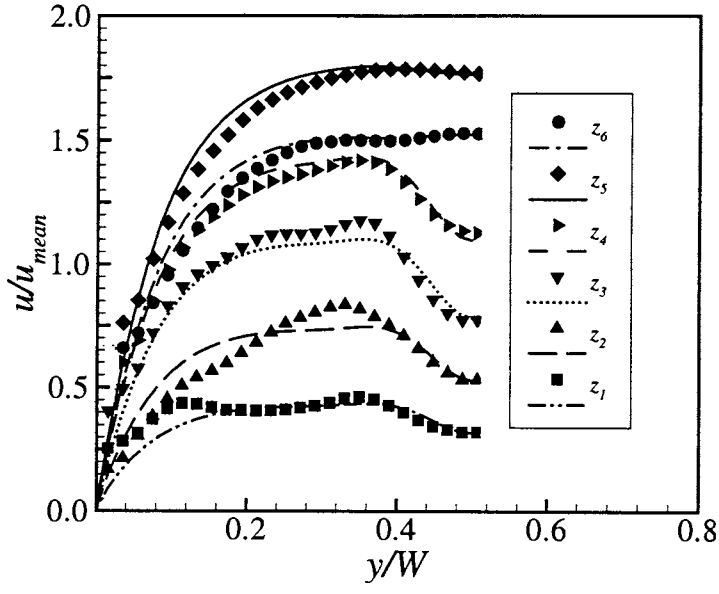

Figure 4.12 Normalized results for Re_{D_h}=431 at 350 μm downstream of microstructure. Experiments - symbols, simulations - lines.

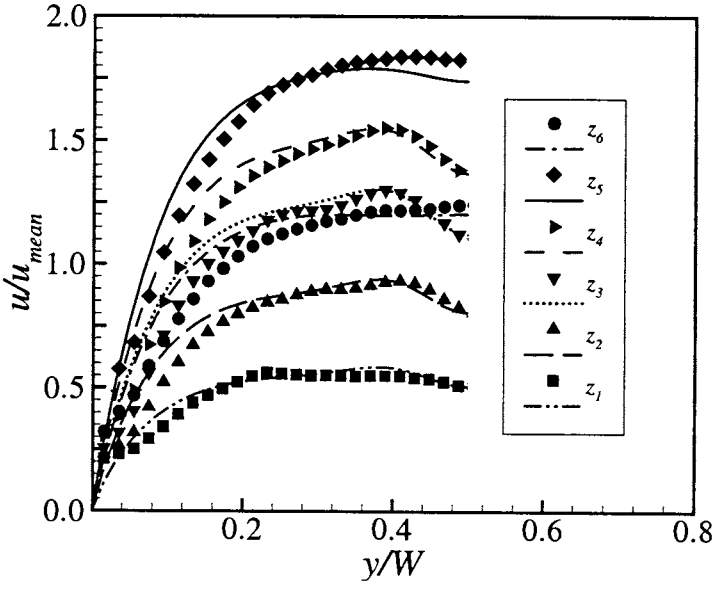

Figure 4.13 Normalized results for Re_{D_h}=431 at 700 μm downstream of microstructure. Experiments - symbols, simulations - lines.

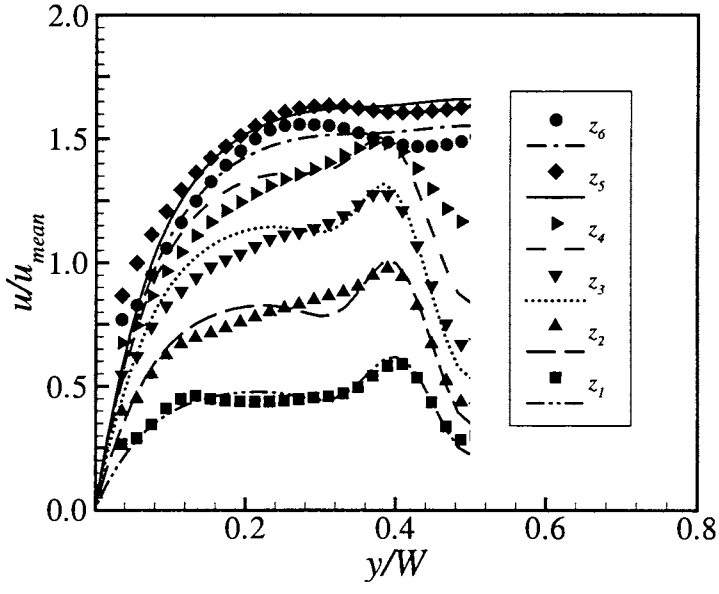

Figure 4.14 Normalized results for Re_{D_h}=1078 at 350 μm downstream of microstructure. Experiments - symbols, simulations - lines.

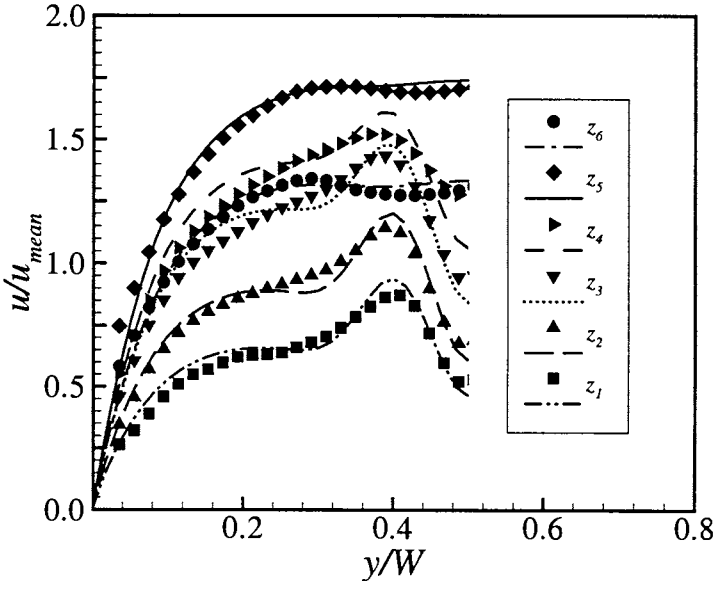

Figure 4.15 Normalized results for Re_{D_h}=1078 at 700 μm downstream of microstructure. Experiments - symbols, simulations - lines.

numerical results at higher flow rates, shows greater discrepancies. Additional sources of error could be attributed to the experimental data acquisition, especially for velocity measurements near the wall, where noise may be significant. However, it is very promising to see good agreement at low Reynolds number flows, which provides the background for the following chapter. Currently, experimental data involving heat transfer within microchannels with microstructures on the interior walls, is not available. The following chapter is a numerical study of microchannel fluid flow past microstructures on the interior wall that include the thermal effects.

5 HYDRODYNAMIC AND THERMAL EFFECTS OF FLOW OVER MULTIPLE STRUCTURES

In MEMS applications where heat removal is necessary, microheat-exchangers and/or microchannel heat sinks are integral parts of the systems. As stated, in Chapter 4, as the surface-area-to-volume ratio decreases, the microchannel internal convection enhances but the pressure required to drive the flow increases significantly. Adding microstructures to the interior walls increases the surface-area-to-volume ratio, while only slightly increasing the pressure needed to drive the flow. The benefit of increasing the surface-area-to-volume ratio without significantly increasing the driving pressure, motivates a better understanding of the effects of microstructures. The chapter herein presents the results from a numerical study of microscale liquid flow over multiple structures, while incorporating heat transfer. Experimental data is not yet available for comparison, however the study simply expands on the hydrodynamic study of Chapter 4. Based on the hydrodynamic study of Section 4.3, only low flow rates will be examined in the following numerical study of thermal effects of fluid flow past microstructures within microchannels.

5.1 Physical Geometry and Considerations

The channels in the present numerical study all share the dimensions of the channel used in the hydrodynamic study of Chapter 4. In addition, multiple microstructure arrays are studied to determine their effect on the hydrodynamic and thermal flow con-

ditions. To allow adequate room for multiple microstructures within the microchannel, the size of the microstructure was reduced to $100 \times 100 \times 43\mu m^3$ ($x \times y \times z$ respectively). Three different microstructure configurations were studied along with one channel absent of microstructures. Figure 5.1 is a schematic of the basic channel without structures. Figure 5.2 illustrates the channel with one single microstructure. Figure 5.3 shows the channel with three structures in a triangular pattern. Figure 5.4 illustrates the channel with the pattern based on channel 3 (Fig. 5.3), repeated 4 times creating an array of microstructures. Each figure presents a view of the channel from the side and top.

In order to model the microchannel flow with heat transfer, a constant heat flux q_s'' was applied to the outer surfaces of the microchannel walls. The experimental analog of a constant heat flux surface condition is wrapping a conducting wire of specified voltage around a microchannel. For the simulations, the constant heat flux is defined to be that of the total power divided by the outer surface area of the microchannel. The computational channel was created with outer walls of negligible thickness, therefore the aforementioned surface area is that of the interior walls of the physical channel.

5.2 Computational Geometry and Numerical Considerations

Similar to the hydrodynamic study of Chapter 4, simulating the full channel is too computationally intensive, therefore the computational channels were reduced in length. One way to reduce the entrance length prior to the microstructure is to use both hydrodynamically and thermally developed profiles. The inlet velocity profile is a simple matter, as discussed in Section 4.1.2, where a fully-developed velocity profile can be specified depending on the flowrate. The thermal profile is not as straightforward because the thermal profile varies with axial position.

It was found with preliminary simulations that the effects of the microstructure only propagated upstream a distance of approximately 200 μm. Based on this prediction, modifications to the microchannels in Figs.5.2 - 5.4 can be made to reduce the entrance

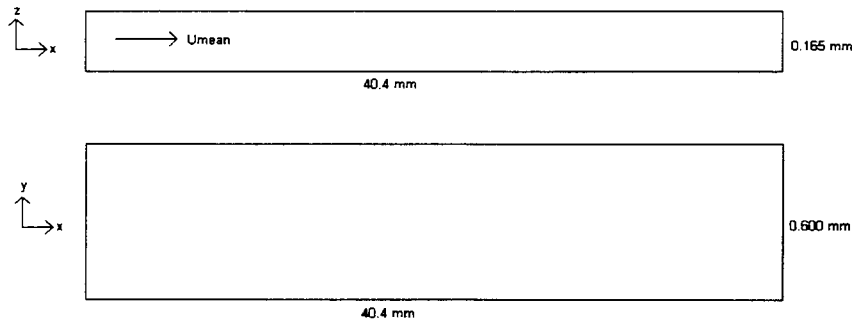

Figure 5.1 Channel 1 with no structures for the side view (x-z) and top view (x-y) (not to scale).

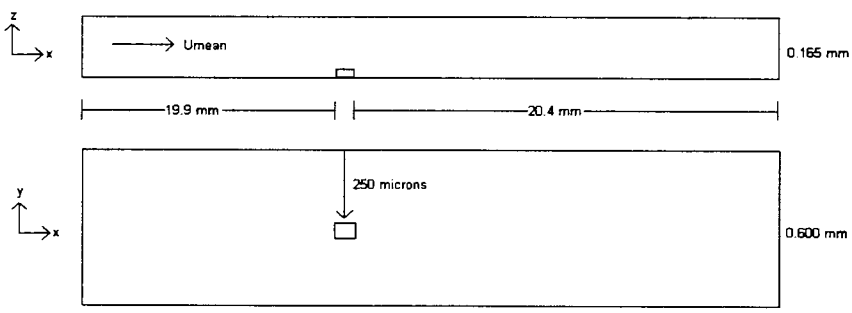

Figure 5.2 Channel 2 with single structure for the side view (x-z) and top view (x-y) (not to scale).

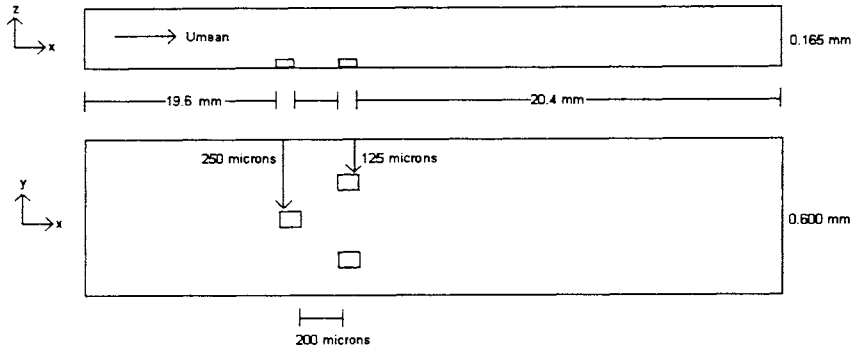

Figure 5.3 Channel 3 with three structures for the side view (x-z) and top view (x-y)(not to scale).

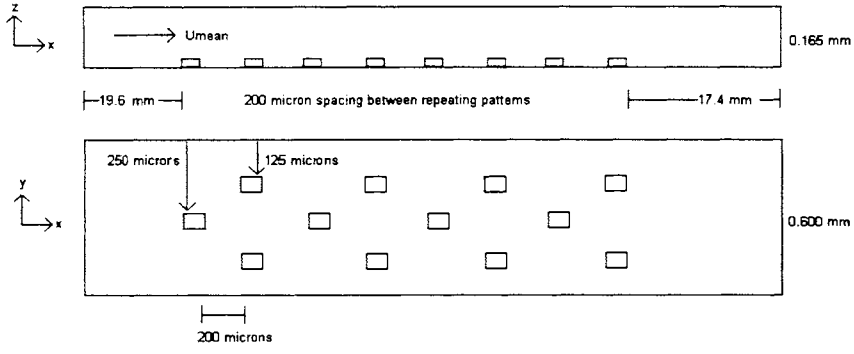

Figure 5.4 Channel 4 with array of repeating three structures for the side view (x-z) and top view (x-y) (not to scale).

length prior to the microstructure. In the figures, the minimum length from the inlet to the first microstructure is 19.6 mm. Since the flow is undisturbed until 200 μm upstream of the microstructure a safe distance of 1600 μm (1.6 mm) was chosen as the new entrance length prior to the microstructure for the simulations. Therefore, the computational inlet is analogous to an x-position of 18 mm on the physical channels shown in Figs.5.1 - 5.4. To obtain the correct inlet boundary conditions (velocity profile and temperature profile) a channel 18 mm long with a constant D_h=258.8 μm was simulated without any microstructures. The outlet profiles from the 18 mm channel were then used as the inlet boundary conditions for the new computational channel, and a check was performed to make sure the flow was thermally fully-developed. Conventional theory states that the thermal entrance length $x_{fd,t}$ for laminar flow is proportional to the hydrodynamic entrance length and the Prandtl number Pr in the following relationship [25]:

$$x_{fd,t} = 0.06 Re D_h Pr = x_{fd,h} Pr \tag{5.1}$$

and for water the Prandtl number, which is a function of temperature, varies between 6 and 9 for the numerical simulations herein. As an additional means to compare the simulations with theory, the mean temperature was examined. The theoretical mean temperature $T_m(x)$ is defined in the following relationship that is valid only for constant heat flux at a surface [25]:

$$T_m(x) = T_{m,i} + \frac{q_s'' P}{\rho Q c_p} x \tag{5.2}$$

where $T_{m,i}(x)$ is the mean inlet temperature, P is the cross-sectional perimeter, Q is the volumetric flowrate, and c_p is the fluid specific heat. The outlet temperature profile from the 18 mm channel was averaged to compare with the theoretical mean temperature $T_m(x = 18 \text{ mm})$. The percent error between the numerical mean temperature and the theoretical mean temperature is 0.53%, thus providing confidence that the exit profile at 18 mm could be used as an inlet condition to simulate fully-developed conditions.

The microstructures were placed along the centerline and/or staggered equal distances in the spanwise direction in order to maintain symmetry. Symmetric conditions permit the use of one-half the width of the physical channel by employing a symmetry boundary condition along the centerplane. The exit length was shortened to reduce the overall size of the problem, but it was kept long enough to allow the flow to return to a fully-developed state, assuring that the exit boundary condition did not adversely affect the solution upstream. The entire length of the computational channel is 10.2 mm, therefore the computational inlet and exit is equivelant to the physical x-locations of 18.0 mm and 28.2 mm respectively. The boundary condition at the interior wall surfaces was set to no-slip (zero velocity).

5.3 Numerical Results and Discussion

Numerical simulations are performed with Re_{D_h} of 50, 100, and 200, as well as, power input of 50, 100, and 200 Watts. It should be noted that changing the power input had no noticeable effects on the velocities, vorticities, and pressures of the numerical simulations herein. Higher power input simply increased the overall temperatures within the channel, which can be seen by the relationship in Eq. 5.2. Therefore, the following discussion only includes data for the 100 Watt simulations. For ease of comparison, some of the results are presented in non-dimensional form. To create non-dimensional variables, the scalar variables were divided by the maximum scalar value within the given case. This allows for the non-dimensional data to fall between 0 and 1, making comparison convenient. An example of the non-dimensionalization is:

$$\zeta^* = \frac{\zeta}{\zeta_{max}} \quad T^* = \frac{T}{T_{max}} \quad P^* = \frac{P}{P_{max}} \tag{5.3}$$

5.3.1 No structure

Figure 5.5 shows the results for Channel 1 (Fig. 5.1) at a Re_{D_h} of 50 and a power of 100 W. The four views shown are for an x - z plane at a y location of 0 (centerplane). The top view shows that the streamlines are horizontal, which is expected since no microstructure is present to disrupt the flow. The second view shows the non-dimensional vorticity magnitudes. Without a structure in the channel, the locations of highest vorticity are near the walls where the shear stress is strongest on the flow. The third view is non-dimensional temperature which shows that higher temperatures are near the walls and the center of the channel has the lowest liquid temperature. The last plane shows the non-dimensional pressure field. Fully-developed laminar flow experiences a constant pressure gradient in the x-direction, and the pressure field is symmetric about the centerplane which can be seen by the equal spacing of the pressure contours.

5.3.2 Single structure

Figure 5.6 shows the non-dimensional results for Channel 2 (Fig. 5.2) at a Re_{D_h} of 50 and a power of 100 W. The top view shows the streamlines over the single structure, capturing the small recirculation region on the downstream side of the structure. The second view is that of vorticity magnitude ζ^* contours, which show the highest vorticity (red) at the upstream top corner of the structure. Downstream of the structure, near the bottom of the channel the vorticity magnitude is very small, similar to the value in the center of the channel where the flow is relatively undisturbed. The third view is that of temperature T^* contours. The recirculation region downstream of the structure is evident by the high temperatures (red) at the bottom corner on the downstream side of the structure. The final view of Fig. 5.6 shows the total pressure P^* contours. The pressure gradient is not constant because the presence of the structure disrupts the flow field, creating a slighter larger pressure upstream and a pocket of low pressure immediately downstream.

Figure 5.7 shows the non-dimensional results for Channel 2 (Fig. 5.2) at a Re_{D_h} of 200 and a power of 100 W. Comparing the results for $Re_{D_h} = 200$ (Fig. 5.7) with those of $Re_{D_h} = 50$ (Fig. 5.6) shows the effects of a higher flow rate in the identical channel. The streamlines in Fig. 5.7 capture a larger recirculation eddy, which is due to the higher flow rate. The higher flowrate causes the vorticity on the top edge of the structure to stretch further downstream along the upper surface of the structure. Again, the temperature is higher at the bottom corner of the downstream side of the structure, however the overall temperatures are lower in magnitude than those of $Re_{D_h} = 50$. Higher flow rates resulting in lower overall temperatures is a trend easily explained by Eq. 5.2. With the flow rate in the denominator of Eq. 5.2, it is clear that a slower liquid velocity results in a higher mean temperature. The pressure contours of $Re_{D_h} = 200$ share a very similar pattern to those of $Re_{D_h} = 50$, with the exception being the magnitude is much higher for higher flow rates.

5.3.3 Multiple structures

Due to the large aspect ratio between channel length and height, only 2 structures are shown in Fig. 5.8 for Channel 4 even though the pattern repeats 4 times. Figure 5.8 shows the streamlines and non-dimensional vorticity, temperature, and total pressure contours for Channel 4 for a $Re_{D_h} = 200$ with 100 W supplied. The repeating pattern results do not display large differences from those of the single structure (Fig. 5.7). The only clear difference is that the streamlines show recirculation regions on the downstream and upstream sides of the microstructures. Otherwise, vorticity, temperature, and pressure fields are similar to the results in Fig. 5.7.

The relationship between flow rate and mean temperature is shown more clearly in Fig. 5.9, which shows a x - y plane at a z-location just below the top of the structures for Channel 4 with 100 W supplied for the three different flow rates. The top view of Fig. 5.9 is that for $Re_{D_h} = 50$, the middle view shows $Re_{D_h} = 100$, and the bottom view

shows $Re_{D_h} = 200$. Since the contour levels of all three views are set to the same scale, it is easy to see that the slower flow rate results in the highest overall temperatures. Likewise, the higher flow rate results in the lower mean temperatures.

Figure 5.10 shows the velocity contours for Channel 4 with 100 W at Re_{D_h} of 50, 100, and 200. The contours show the higher velocity locations between the wall and the structures and also between the structures near the center of the channel. The flow speeds up as it "snakes" around and between the microstructures. The flow patterns near the microstructures are examples of laminar flow exhibiting turbulent-like characteristics. Turbulent characteristics are very desirable because they aid in overall heat transfer and mixing.

A comparison of the three different channels is shown in Figures 5.11 and 5.12 for contours of temperature and total pressure, respectively. All three cases shown are that of $Re_{D_h} = 100$ with 100 W supplied. The top view is for Channel 2 (Fig. 5.2), the middle view shows Channel 3 (Fig. 5.3), and the bottom view is Channel 4 (Fig. 5.4) of the x - y plane at a z-location just below the top of the structures. The temperature contours in Fig. 5.11 show the enhanced heat transfer by the dissipation of energy for the repeating structure channel. Channel 4 shows higher temperatures along the centerline compared to the other channels. Likewise, the total pressure is higher near the repeating structures of Channel 4, as shown in Fig. 5.12. The higher pressure region upstream of the repeating structures is expected since the multiple structures interfer with the flow creating larger pressures needed to drive the flow over and around the structures.

5.3.4 Static pressure gradients

It can be seen in Fig. 5.12 that total pressure increases upstream of the structures when more structures are present. When sizing a pumping force in an industrial application, it is the static pressure drop that must be overcome to drive the flow. Therefore, this section discusses the results pertaining to the static pressure drops for the different

Table 5.1 Pressure gradient results for 4 channels at $Re_{D_h} = 100$ with 100 W supplied.

channel	$\partial p/\partial x$(Pa/m)	% increase
1	208824	–
2	210160	0.64%
3	212790	1.90%
4	224218	7.37%

channels. Examining the cases of $Re_{D_h} = 100$ with a power of 100 W supplied, the static pressure drops were calculated by taking the difference between the outlet and inlet pressures and dividing by the total domain length of 10.2 mm. The static pressure gradient results are shown in Table 5.1 The third column of Table 5.1 shows the percent increase in pressure gradient compared to that of a simple channel without any structures (Fig. 5.1). By repeating the 3 structure pattern a total of 4 times, the pressure gradient increased 7.37%. When compared to the pressure increase created by reducing the hydraulic diameter (refer to Chapter 4), adding an array of microstructures is a desirable method of increasing the surface-area-to-volume ratio.

5.4 Summary

Clearly, adding microstructures to the interior wall of a microchannel increases the surface-area-to-volume ratio, while only slightly increasing the pressure needed to drive the flow. The pressure increase due to adding microstructures, has less of a impact than the increased pressure from decreasing the hydraulic diameter. It is evident that even low Reynolds number flows (laminar regime) can be disrupted by microstructures in order to create "turbulent-like" characteristics. The resulting recirculation and voriticity provide laminar flows with greater heat transfer and mixing.

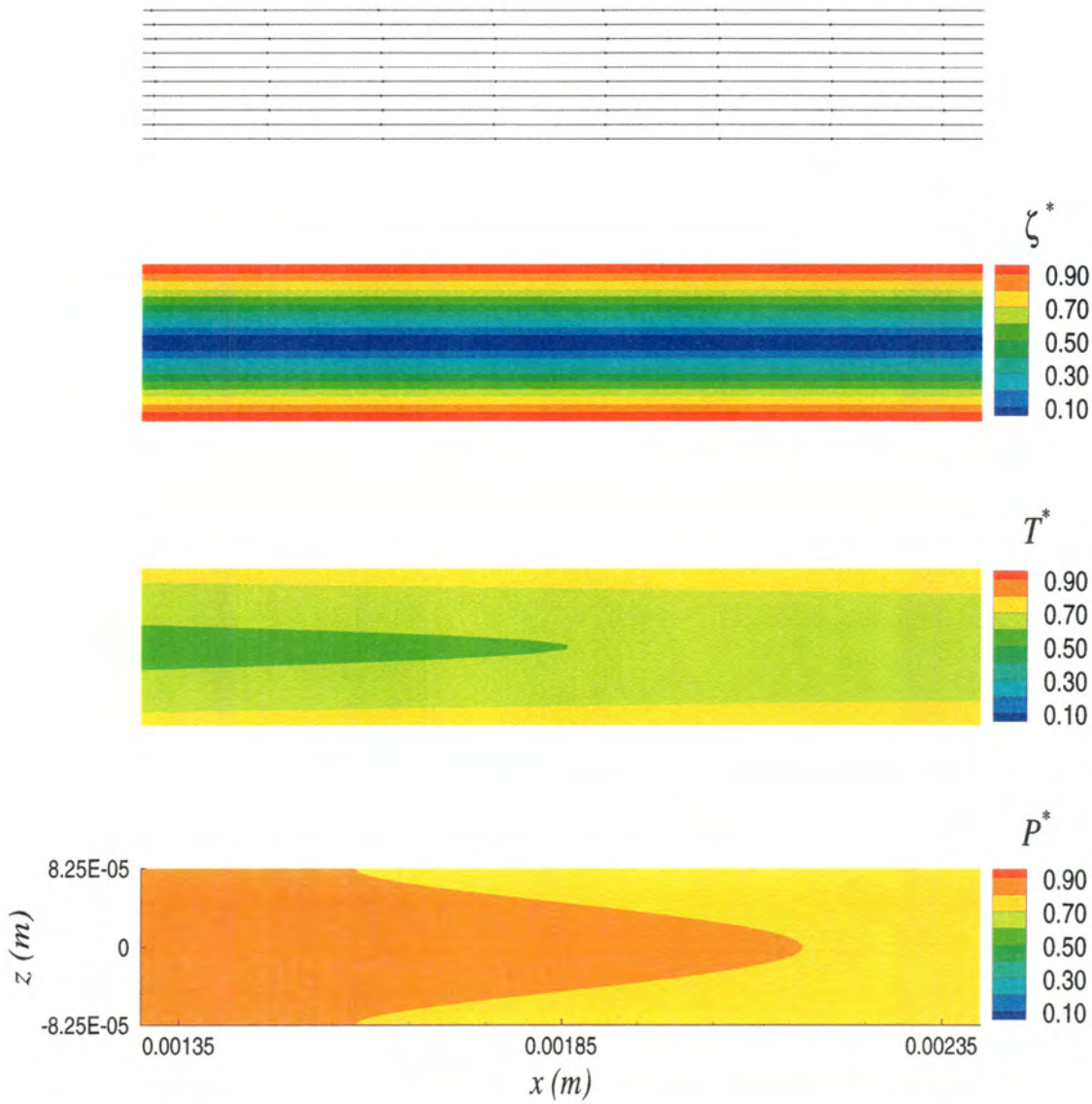

Figure 5.5 Streamlines and non-dimensional contours: vorticities, temperatures, and total pressures for Channel 1 $Re_{D_h} = 50$ with 100 W supplied.

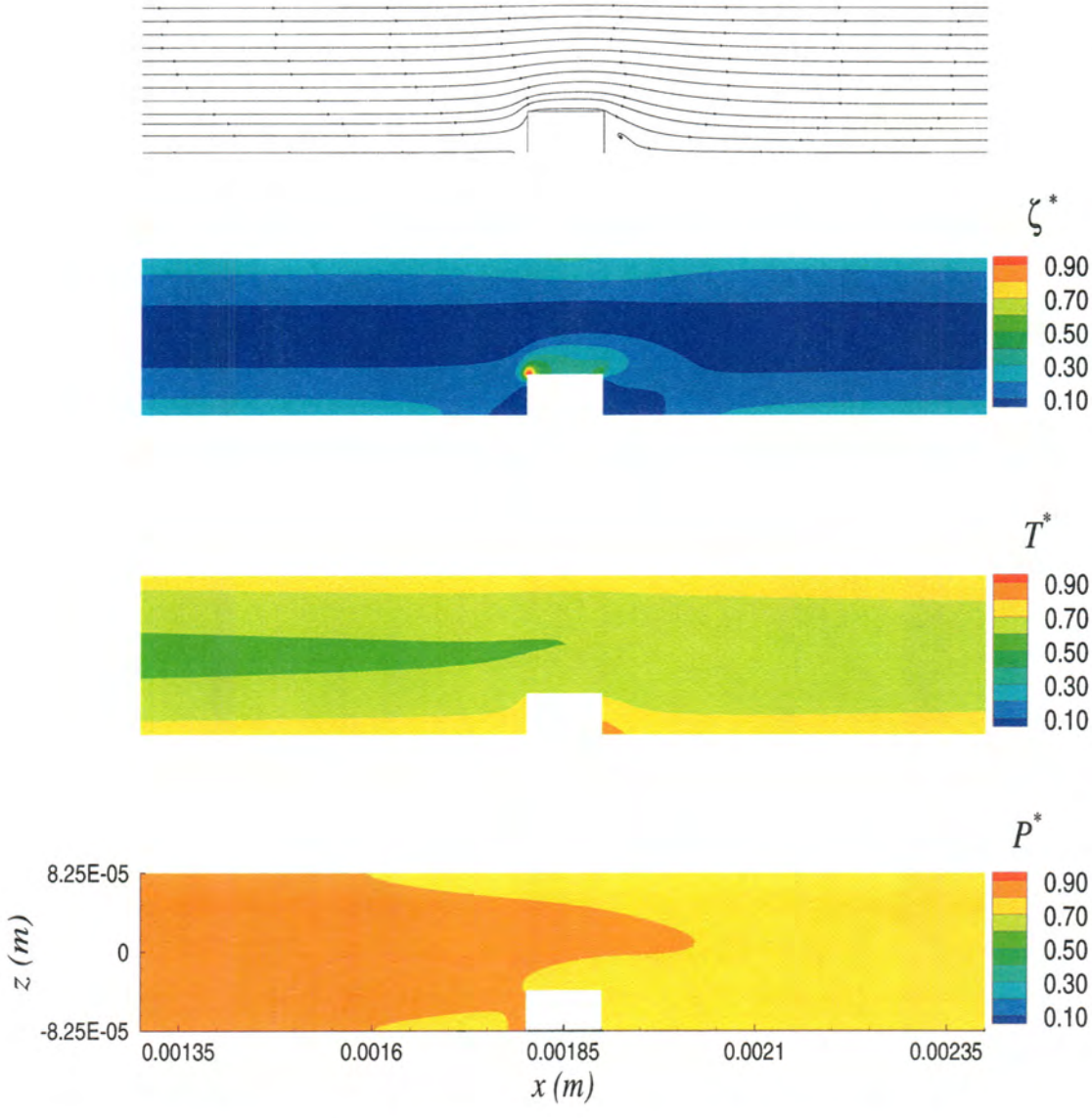

Figure 5.6 Streamlines and non-dimensional contours: vorticities, temperatures, and total pressures for Channel 2 $Re_{D_h} = 50$ with 100 W supplied.

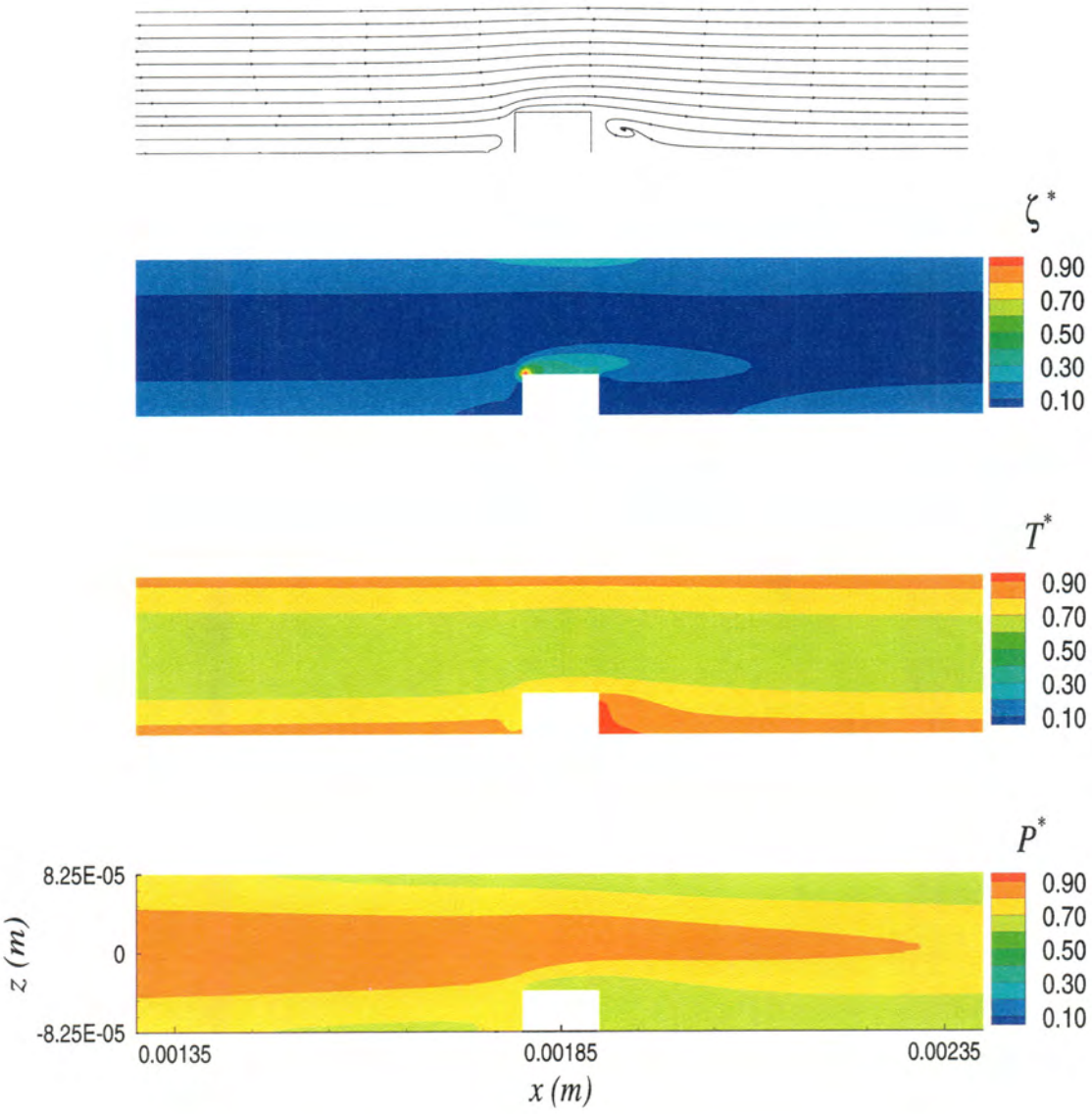

Figure 5.7 Streamlines and non-dimensional contours: vorticities, temperatures, and total pressures for Channel 2 $Re_{D_h} = 200$ with 100 W supplied.

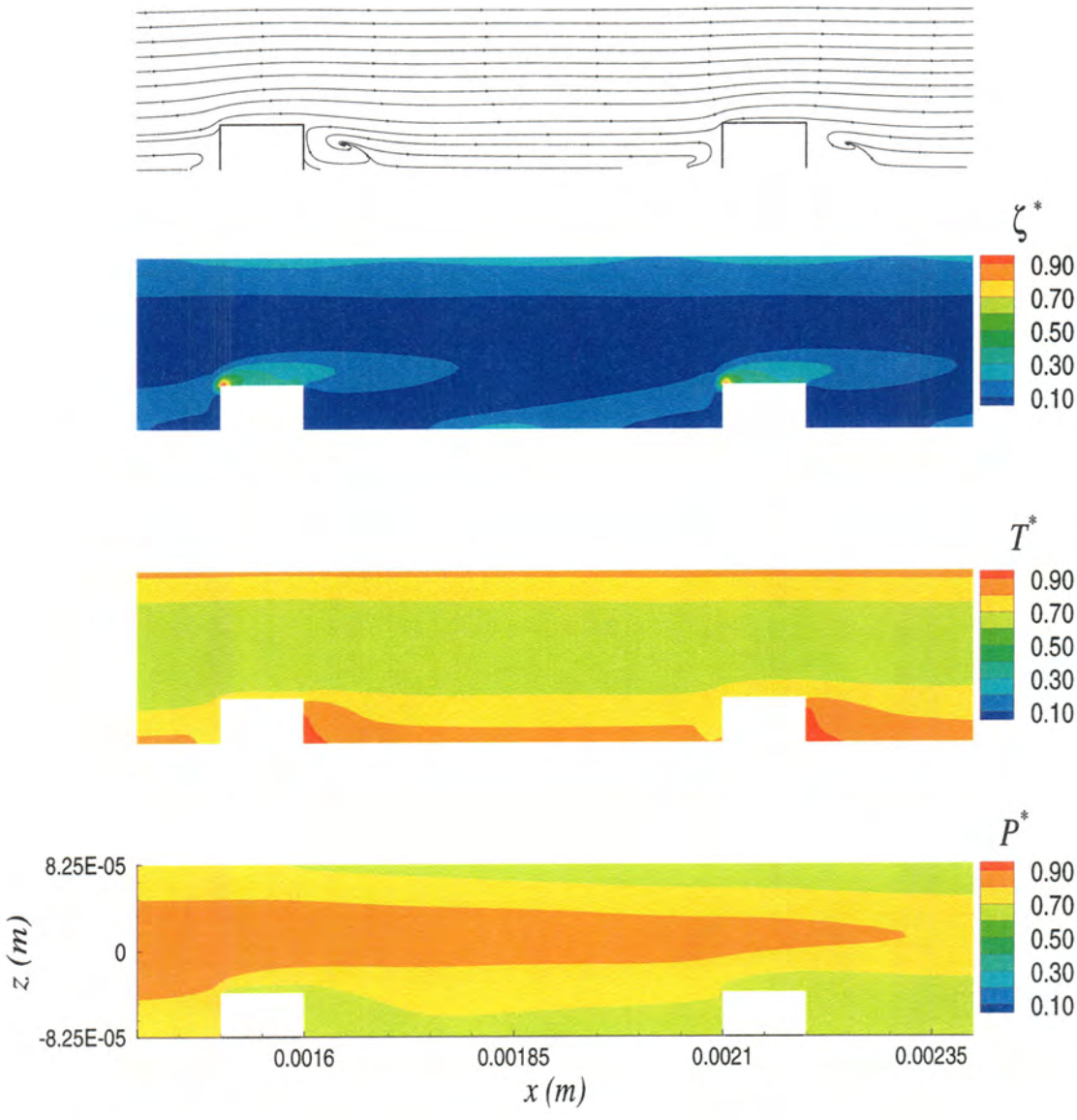

Figure 5.8 Streamlines and non-dimensional contours: vorticities, temperatures, and total pressures for Channel 4 $Re_{D_h} = 200$ with 100 W supplied.

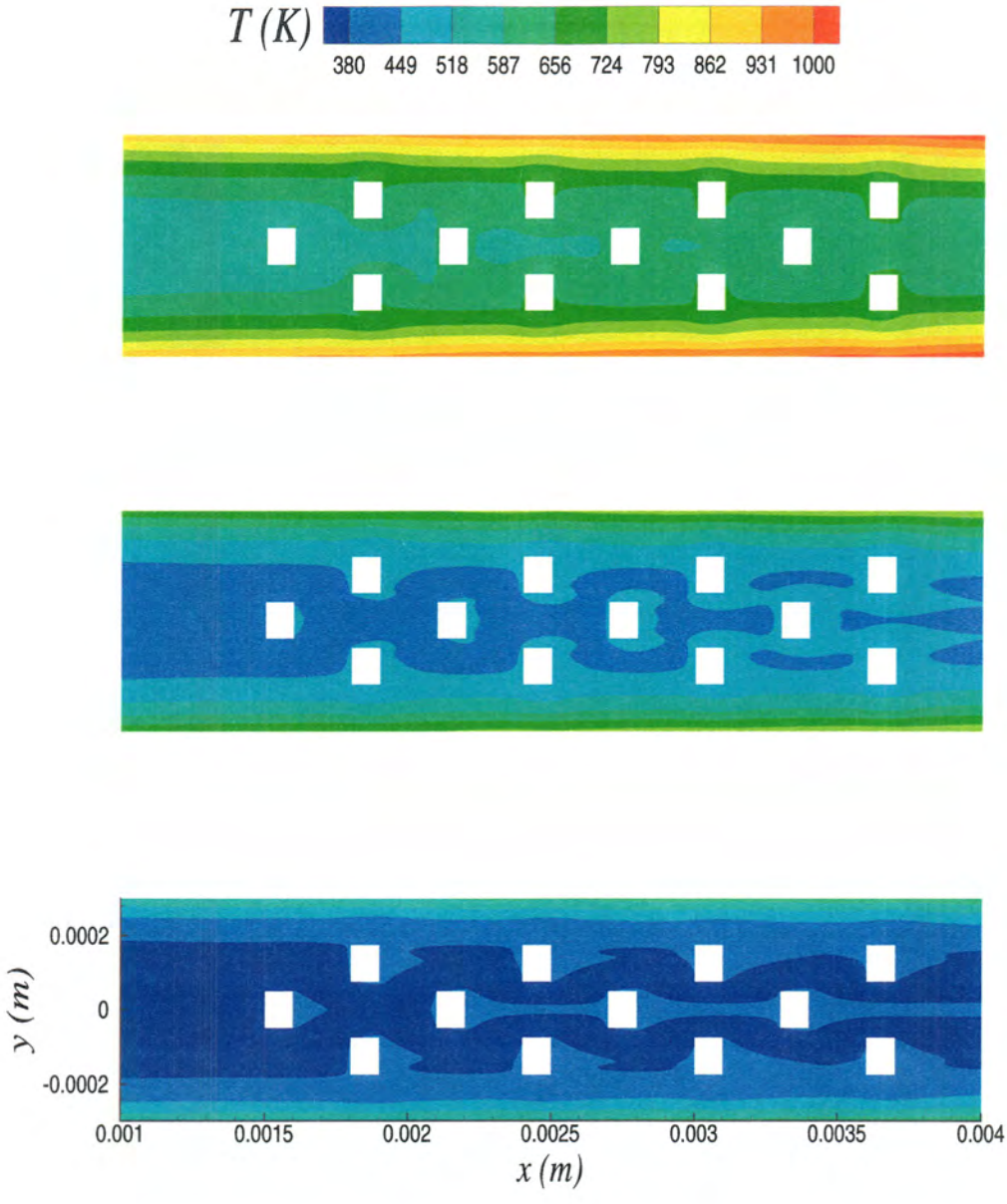

Figure 5.9 Channel 4 temperature contours for $Re_{D_h} = 50$, 100, and 200 with 100 W supplied.

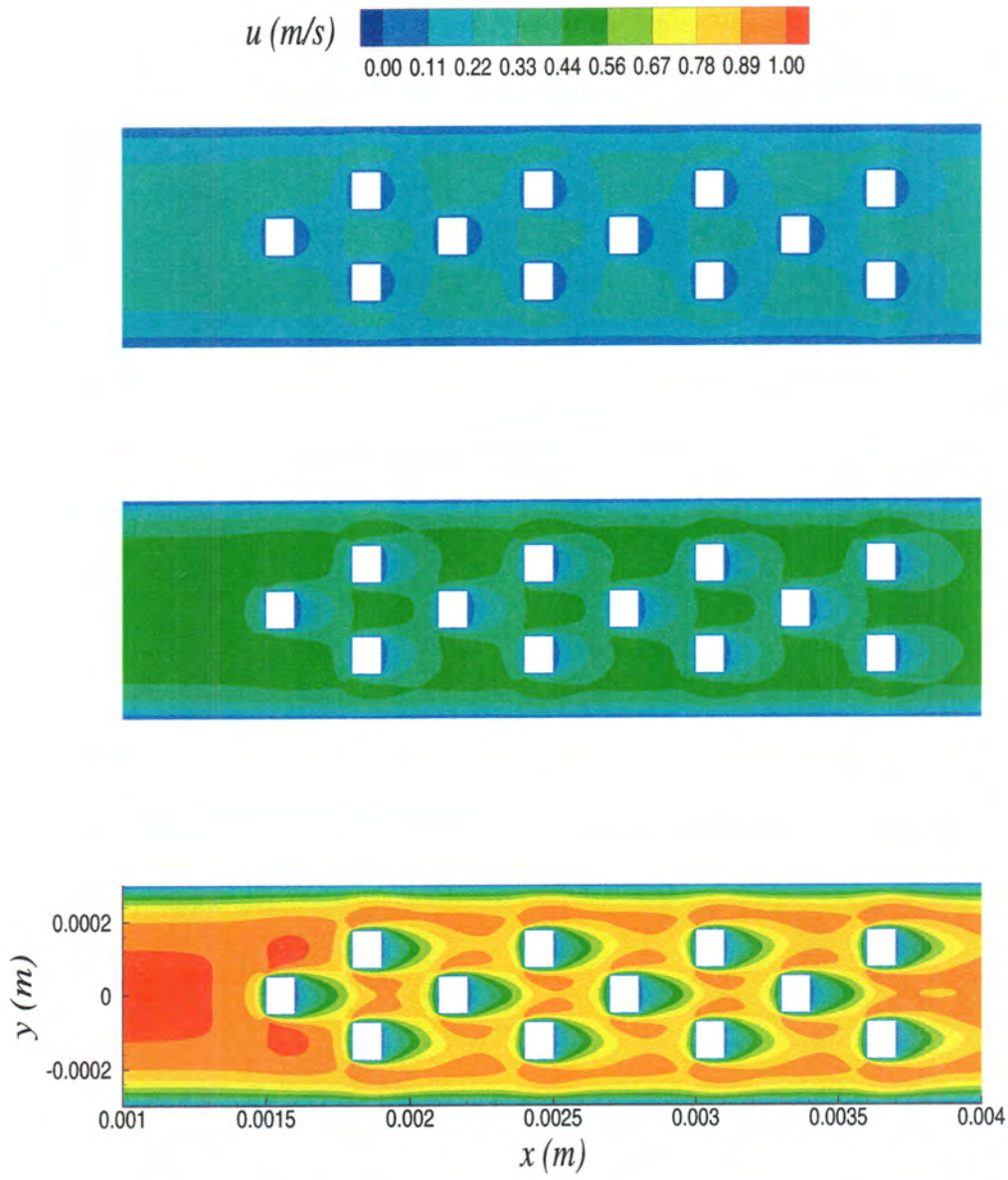

Figure 5.10 Channel 4 velocity contours for $Re_{D_h} = 50$, 100, and 200 with 100 W supplied.

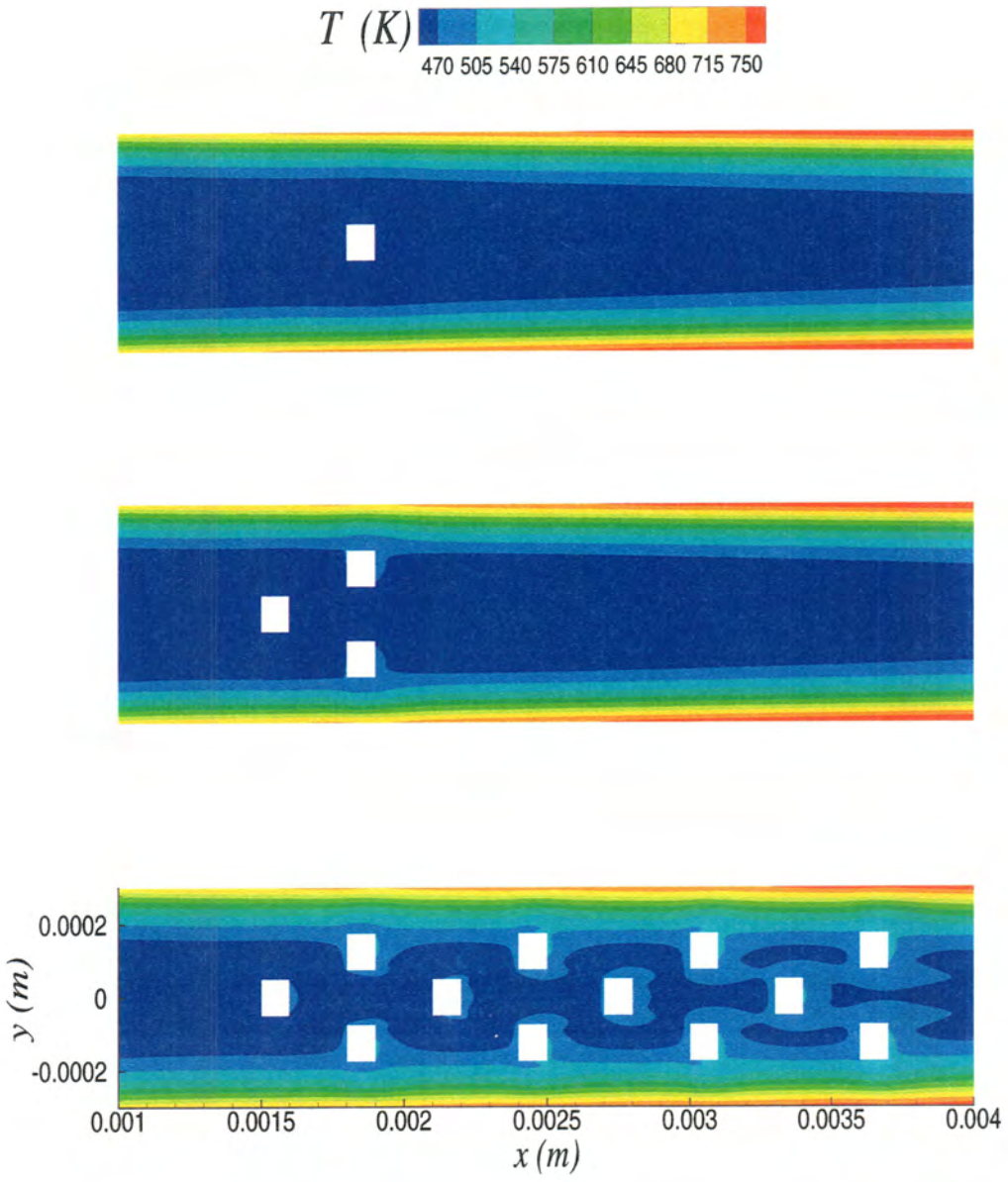

Figure 5.11 Channels 2,3, and 4 temperature contours for $Re_{D_h} = 100$ with 100W supplied.

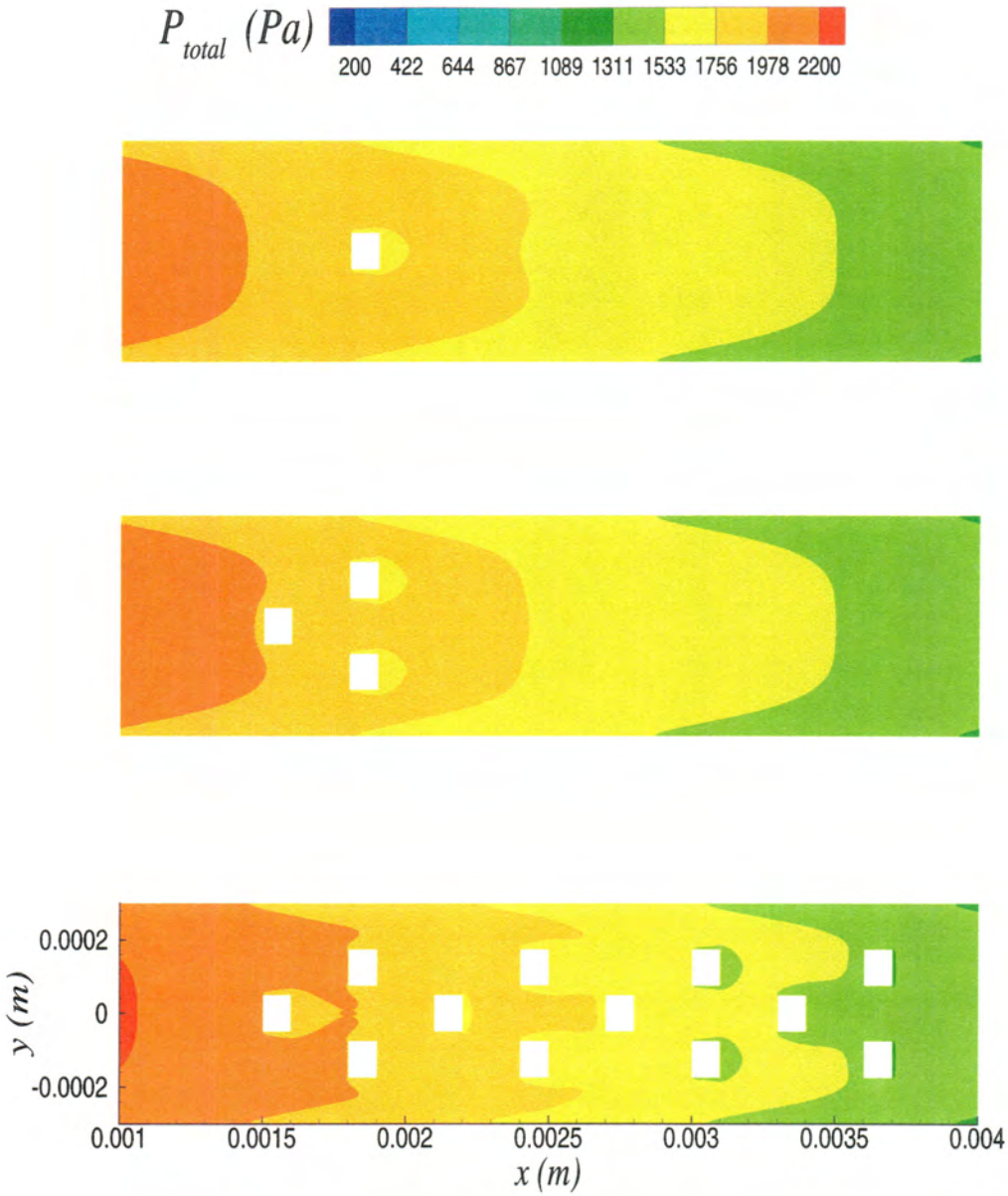

Figure 5.12 Channel 2,3, and 4 total pressure contours for $Re_{D_h} = 100$ with 100W supplied.

6 CONCLUDING REMARKS AND FUTURE RECOMMENDATIONS

The hydrodynamic and thermal effects of liquid flows on the microscale were numerically studied to provide a more in-depth understanding of observed complex phenomena. Of particular interest was the analysis of incorporating microstructures in a microchannel to increase the surface-area-to-volume ratio. The use of microstructure arrays has the potential to enhance convective heat transfer without sacrificing or requiring larger pressures to drive the flow. The commercial code Fluent 6.0 was used in the research, and specific issues regarding surface boundary conditions were addressed while assessing the validity of using the code for microscale fluid simulations.

The grid creation and numerical simulations were completed using the commercial software, Gambit 2.0 and Fluent 6.0 respectively. Fluent 6.0 uses a finite-volume segregated solver implicit method employing the SIMPLE pressure correction approach. All numerical simulations were steady-state laminar flows of liquid through microchannels. The no-slip boundary condition was applied to all fluid-surface boundaries, and fully-developed velocity profiles were used as the inlet velocity boundary condition. The microchannel exit boundary condition of atmospheric pressure was employed for all simulations. The numerical simulations were performed at Iowa State University on the Intel Xeon cluster (44 node machine with 2.8 Ghz dual processors per node).

Preliminary numerical efforts focused on benchmarking numerical results to experimental data from different studies including the fluid-surface boundary condition for microchannels of either hydrophilic or hydrophobic channel walls. The no-slip boundary

condition was shown to be applicable for flows over a hydrophilic surface. Good agreement between the numerical, analytical, and experimental results for liquid flows over a hydrophilic surface was shown. Flow over a hydrophobic surface showed a finite-slip velocity equal to 10% of the free-stream, which is significant on the microscale, however numerical simulations were not attempted for flow over a hydrophobic surface. Experimental friction factors for fluid flows through different sizes of microtubes over a range of Reynolds numbers were compared to numerical and analytical results. The experimental surface roughness results showed that the conventional laminar friction factor relationship ($fRe = 64$) can be inaccurate by as much as 25% in microscale liquid flows. The numerical results incorporated the conventional Navier-Stokes equations which neglect surface roughness for laminar flow, therefore, the numerical results were equal to the conventional theory showing the same error with the experimental results.

A numerical study of the hydrodynamic effects of flow over a microstructure was completed and the results were compared to experimental data acquired using microscopic particle image velocimetry. The study of hydrodynamic effects of flow over a single microstructure showed very good agreement between numerical and experimental results, especially at low Reynolds numbers. The wake effect introduced by the presence of the microstructure was captured well by both the numerical and experimental data. At higher flow rates, the error between the simulations and experiments was larger. This could be due to the conventional laminar numerical formulation, as well as the difficulty in obtaining experimental results in microchannels with high flow rates. The good agreement of the hydrodynamic study at low rates led to the numerical study of thermal effects of low Reynolds number flows over multiple microstructures. The results showed that an array of microstructures created enhanced heat dispersion, recirculation regions around the structures, while only slightly increasing the pressure needed to drive the flow.

A microchannel with an array of microstructures could some day be an integral part of

micro-cooling system incorporated into MEMS. Future work recommendations include comparing the numerical results of thermal effects to experimental data. In addition, studying different array sizes and patterns could lead to valuable information regarding the relationship between enhanced heat transfer and increased surface area. A more closely packed array of microstructures will allow the wake effects from neighboring structures to interfere with one another, therefore creating even more disruption to the flow. One could perform a study to obtain the optimal microstructure packing which achieves the most heat transfer without sacrificing a large pressure increase. Another grid resolution study should be performed to make sure the solution is still grid independent after thermal effects are incorporated. Incorporating a viscosity that is a function of temperature will give rise to a study on how increasing the power supplied affects the hydrodynamics. A quantitative study of heat transfer coefficients (average value from computational inlet to outlet) will provide direct indications of the heat transfer performance, and can be compared to values of straight channels without microstructures to indicate "heat-sinking power" of the different array configurations. It is unlikely that water would be the most effective fluid in industrial applications; therefore a parametric study employing different working fluids, as well as different microchannel materials could lead to valuable information to aid industry in the production and design of MEMS.

Bibliography

[1] DeGaspari, J., Mixing It Up, *ASME Mechanical Engineering*, **125**(8):34–38 (2003).

[2] Battaglia, F., Olsen, M., Li, H., Tworek, A., Bondar, F., and James, K., Experimental and Computational Results for Flow Around a Single Microstructure in a Microchannel, *Journal of MEMS*, (In review, 2004).

[3] DeGaspari, J., MEMS' Rocky Road, *ASME Mechanical Engineering*, **124**(6):38–41 (2002).

[4] Gad-el Hak, M., The Fluid Mechanics of Microdevices – The Freeman Scholar Lecture, *Journal of Fluids Engineering*, **121**:5–33 (1999).

[5] Guo, Z.Y. and Li, Z.X., Size Effect on Single-Phase Channel Flow and Heat Transfer at Microscale, *International Journal of Heat and Fluid Flow*, **24**:284–298 (2003).

[6] Koplik, J., Molecular Dynamics of Fluid Flow, *Research Trends in Fluid Dynamics*, American Institute of Physics, New York, 1996.

[7] Zhuang, Y., Ma, C.F., and Qin, M., Experimental Study on Local Heat Transfer with Liquid Impingement Flow In Two-Dimensional Micro-Channels, *International Journal of Heat and Mass Transfer*, **40**(17):4055–4059 (1997).

[8] Beskok, A. and Karniadakis, G.E., Simulation fo Heat and Momentum Transfer in Complex Microgeometries, *Journal of Thermophysics and Heat Transfer*, **8**(4):647–655 (1994).

[9] Lee, S.Y.K., Wang, M., and Zohar, Y., Gas Flow in Microchannels with Bends, *Journal of Micromechanics and Microengineering*, **11**:635–644 (2001).

[10] Colin, S., Lalonde, P., and Caen, R., Validation fo a Second-Order Slip Flow Model in Rectangular Microchannels, *Heat Transfer Engineering*, **25**(3):23–30 (2004).

[11] Munson, B.R., Young, D.F., and Okiishi, T.H., *Fundamentals of Fluid Mechanics*, John Wiley and Sons, Inc. Publishing, New York, 1998.

[12] Xu, B., Ooi, K.T., and Wong, N.T., Experimental Investigation of Flow Friction For Liquid Flow in Microchannels, *International Journal of Heat and Mass Transfer*, **27**(8):1165–1176 (2000).

[13] Xu, B., Ooi, K.T., Wong, N.T., and Liu, C.Y., Study on the Viscosity of the Liquid Flowing in Microgeometry, *Journal of Micromechanics and Microengineering*, **9**:377–384 (1999).

[14] Koo, J. and Kleinstreuer, C., Liquid Flow in Microchannels: Experimental Observations and Computational Analyses of Microfluidics Effects, *Journal of Micromechanics and Microengineering*, **13**:568–579 (2003).

[15] Tretheway, D. and Meinhart, C., Apparent Fluid Slip at Hydrophobic Microchannel Walls, *Physics of Fluids*, **14**(3):L9–L12 (2002).

[16] Peng, X.F. and Peterson, G.P., The Effect of Thermofluid and Geometrical Parameters on Convection of Liquids Through Rectangular Microchannels, *International Journal of Heat and Mass Transfer*, **38**(4):755–758 (1995).

[17] Wu, H.Y. and Cheng, P., An Experimental Study of Convective Heat Transfer in Silicon Microchannels with Different Surface Conditions, *International Journal of Heat and Mass Transfer*, **46**:2547–2556 (2003).

[18] Koo, J. and Kleinstreuer, C., Viscous Dissipation Effects in Microtubes and Microchannels, *International Journal of Heat and Mass Transfer*, **47**:3159–3169 (2004).

[19] Nakayama, W., Ohba, Y., and Maeda, K., The Effects of Geometric Uncertainties on Micro-Channel Heat Transfer – A CFD Study on the Tilted-Cover Problem, *Heat Transfer Engineering*, **25**(1):50–60 (2004).

[20] Lockett, M., Simmons, M.J.H., and Kendall, K., CFD to Predict Temperature Profile for Scale Up of Micro-Tubular SOFC Stacks, *Journal of Power Sources*, **131**:243–246 (2004).

[21] Wang, H., Iovenitti, P., Harvey, E., and Masood, S., A Simple Approach for Modelling Flow in a Microchannel, *Proceedings of SPIE*, **4236**:99–106 (2001).

[22] Incorporated, Fluent, *Gambit 2.0 and Fluent 6.0 User's Manual*, Fluent, Inc., Labanon, New Hampshire, 2001.

[23] Anderson, D.A., Tannehill, J.C., and Pletcher, R.H., *Computational Fluid Mechanics and Heat Transfer*, Hemisphere Publishing Corporation, New York, 1984.

[24] White, F.M., *Viscous Fluid Flow*, McGraw Hill Publishing, Boston, Massachusetts, 1991.

[25] Incropera, F.P. and DeWitt, D.P., *Fundamentals of Heat and Mass Transfer*, John Wiley and Sons, Inc. Publishing, New York, 2002.